Contents

List of Figures

Chapter 4

Results

In this chapter I will present and discuss the results obtained from the multi–frequency VLBI observations of NGC 1052. I will start with the presentation of the VLBI images (Section 4.1), produced from the self–calibrated (u, v)-data. The pre-analysis of these images will include the alignment and modeling of the VLBI structure of NGC 1052 at the four observed frequencies (Section 4.2). In Section 4.3, the spectral properties of NGC 1052 and the various components in the jets will be discussed. A method to obtain source information from the brightness temperature distribution across the source will be presented and applied in Section 4.4 . The polarimetric properties of NGC 1052 on VLBI scales will be reported, for the first time, in Section 4.5 . In Section 4.6, an analysis of the core-shift of the two jet–cores with respect to frequency will be performed.

4.1 Total intensity mapping

Figure 4.1 shows the total intensity images, produced with the hybrid mapping software DIFMAP (Pearson et al. 1994), as described in Chapter 3. The main characteristics of the source visible in these images, which are described in the following, are summarized in Table 4.1. Table 4.2 gives the map parameters.

The basic features in the VLBI structure of NGC 1052 are two oppositely directed jets divided by an emission gap in between. These are visible in the 5 and 8.4 GHz map with a resolution of about 3 and 2 mas, respectively. At 5 GHz structures out to about 30 mas from the gap on both sides can be seen. At 8.4 GHz, emission out to about 14 mas on both sides from the gap is visible.

At both frequencies, the source geometry can be described by a position angle (P.A.) of approximately 65° (−155° for the western jet)[1]. The source exhibits a kink about 8 mas east from the gap, where the eastern jet turns slightly to the north and back to its old direction some milliarcseconds further out. Although not that pronounced, this kink is visible as well in the 8.4 GHz map at the same distance from the gap.

The 22 GHz image shows the inner part of the eastern jet out to 6 mas from the gap and a slightly shorter western jet out to about 4 mas from the gap both with submilliarcsecond resolution. Marginally detected emission is spread out to 13 mas in the eastern jet and to 6 mas on the western side. The eastern jet seems to be slightly curved on this scale with the P.A. changing smoothly from 67° to 83° (counterclockwise, in contrast to the behavior

[1] The P.A. is measured from north through east.

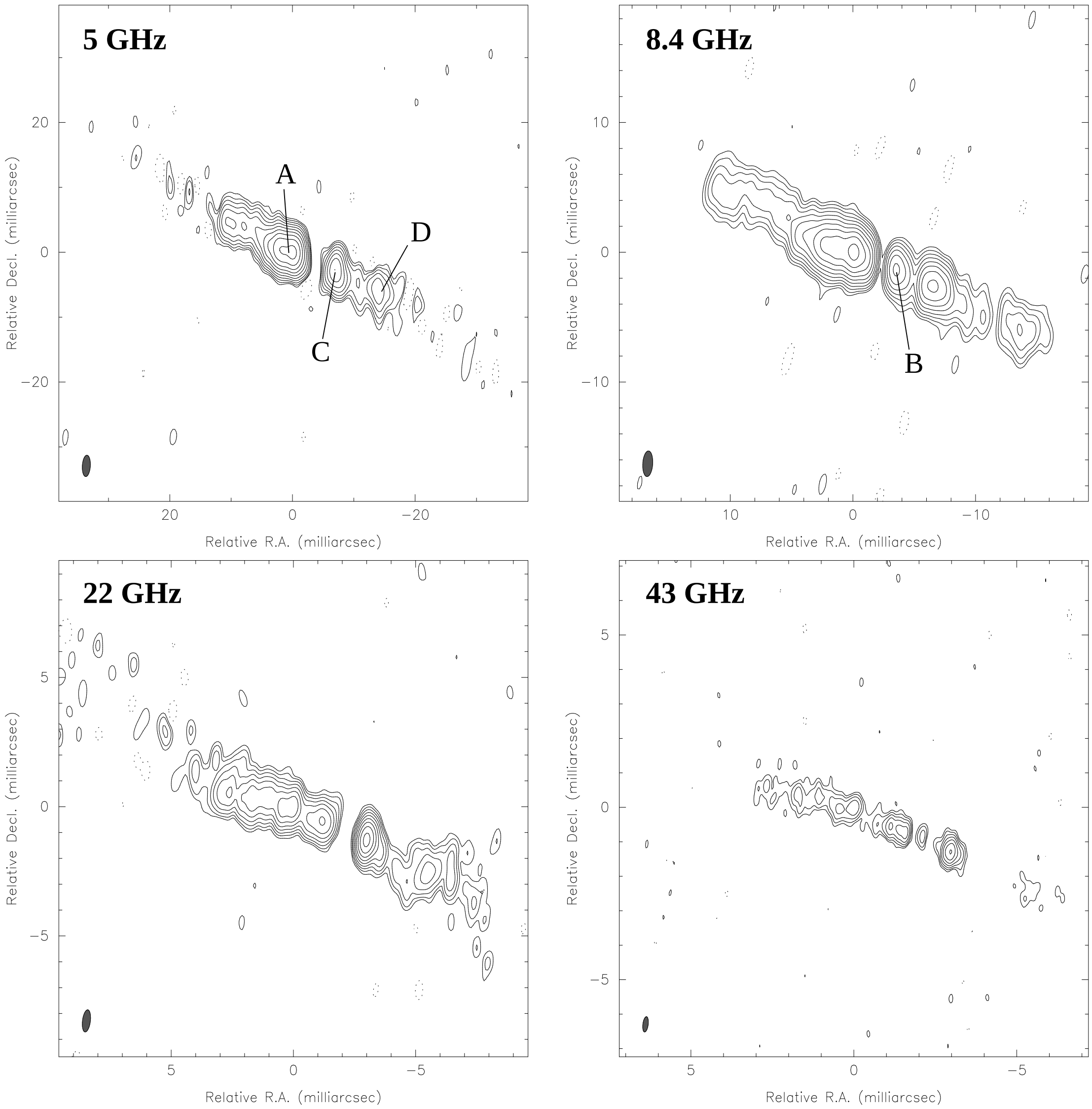

Figure 4.1: Contour plots of the total intensity flux of NGC 1052 at the observed frequencies. The convolution beams are shown at the bottom left corner of each map. Table 4.1 summerizes the source characteristics at each frequency and Table **??** gives the map parameters. Note the different map scales at the different frequencies.

at the kink further out at lower frequencies). The western jet shows strong curvature. From the very prominent core (component B) the outflow has an initial position angle of $-140°$. At 3 mas from the gap the position angle changes by $90°$ to $-50°$ followed by a slower curvature towards the P.A. of $-155°$, visible at the lower frequency maps.

The 43 GHz image could be misinterpreted, if it had been obtained from a single frequency observation, as a one–sided source with a strong core and only marginal emission on the counterjet side. The comparison with the 22 GHz image, however, ascribes this strong core (component B) to the western jet (look for details at the model fitting and the core–shift analysis results in Section 4.2 and 4.6) and the curved structure in the east of it to the eastern jet. The curvature is consistent with the 22 GHz map but emission is only visible out to 5 mas from the gap. The angular resolution achieved here is about 0.5 mas (see table 4.2 for the exact map parameters).

The angular distance measurements in this paragraph are based on the interpretation of component B as the core of the western jet and the gap position between it and the next component on its east side at 43 GHz. This interpretation will be tested and discussed in more detail in Section 4.6 but seems reasonable even at this point of the analysis.

The jets appear nearly symmetric in the 5 GHz and 8.4 GHz maps, symmetry becoming less prominent at higher frequencies. At 43 GHz the eastern jet appears very rich in detail while in the western jet only two components remain detectable above the noise level. The emission gap is most prominent at 5 GHz. The maps at 8.4, 22 and 43 GHz reveal jet components occupying the region where the gap is located at 5 GHz, leaving a smaller but still prominent gap–region left. The eastern jet appears rather continuous with a strong inner region (labeled as component A) and fainter emission further out from the center of symmetry. The western jet has a much more fragmentary structure. It seems to be composed of single "blobs" which are unresolved and partly blended at low frequencies.

It is not easy to identify the single components at different frequencies. Especially between 5 and 8.4 GHz the identification is problematic because the higher frequency map shows a larger number of components than the lower frequency one. Although this problem cannot be overcome just by a visual inspection of the maps (but the next section will deal with the topic of alignment) there are hints for an alignment, which identifies the innermost part of the western jet at 5 GHz (component C) with the second component from the gap at 8.4 GHz. The core of the western jet (component B) is too weak to be detectable at 5 GHz but becomes more and more dominant at higher frequencies. At 8.4 GHz it occupies nearly the whole 5 GHz–gap region.

Table 4.1: Source characteristics on mas-scales

ν	Mean P.A.	eastern jet extension	western jet extension	Gap region	Notes
5 GHz	$\sim 65°$	30 mas	30 mas	prominent, $\sim$1.25 mas	A dominates; B totally absorbed; kink, 8 mas east of the gap
8.4 GHz	$\sim 65°$	14 mas	14 mas	nearly closed	A dominates; B occupies the 5 GHz gap-region; kink, 8 mas east of the gap
22 GHz	$\sim 67°$	13 mas	6 mas	prominent, $\sim$0.45 mas	B dominates; curved eastern jet (P.A.ϵ [67°,83°]); heavy bending of the western jet
43 GHz	$\sim 70°$	5 mas	3.5 mas	$\sim$0.2 mas	B dominates; curved eastern jet (P.A.ϵ[67°,83°]

Table 4.2: Total intensity map parameters

ν [Hz]	λ [cm]	beam [mas $\times$ mas,°]	$S_{\rm peak}$ [Jy/beam]	$S_{\rm tot}$$^{(a)}$ [Jy]	rms [mJy/beam]	Contours^{d} [mJy/beam]
5	6	3.30 × 1.31,–3.74	0.660 ^{b}	2.41	0.26	0.99 × (-1,1,2,4,...,256,512)
8.4	4	1.98 × 0.81 ,–3.87	0.538 ^{b}	2.39	0.25	0.81 × (-1,1,2,4,...,256,512)
22	1.3	0.86 × 0.32 ,–7.63	0.339 ^{c}	1.51	1.20	1.02 × (-1,1,2,4,...,128,256)
43	0.7	0.45 × 0.16 ,–7.93	0.126 ^{c}	0.67	0.67	1.89 × (-1,1,2,4,...,16,32,64)

[a] Total flux density recovered in the map model; [b] Corresponds to the A component; [c] Corresponds to the B component; [d] Contours in Figure 4.1 (There are more maps in the following sections with different contours).

4.2 Model fitting and image alignment

In VLBI imaging the absolute positional information is lost in the phase-calibration process. In the case of simultaneous multi-frequency observations this means that *a–priori* it is not clear how the images at the different frequencies have to be aligned. The ideal method for overcoming this is to carry out phase-referencing observations, using a compact nearby object and using it to calculate the position of the target source relative to it. Our VLBA observations were not phase-referenced, so another way was used to register the four maps. For this a model fitting of the visibilities with circular[2] Gaussian components was performed.

The aim of model fitting is to find a simple parametrization of the data using only a few model components which should be identifiable with characteristic features in the total intensity images. A pairwise identification of the model components between adjacent frequencies then allows to register the images. As another benefit the spectra of the model components can be derived.

The model fitting was performed in DIFMAP in a very similar way to the CLEANing and phase self-calibration process (without amplitude calibration) of the total intensity maps. The (uv)–data was approximated in a first step by just one model component in the phase center in varying its full width at half maximum (FWHM) and the contained flux density. Then the residual map was inspected and a second model component was added at the position of the largest residual. This second component was set to be variable in flux density, position and diameter. DIFMAP allows to vary these parameters in order to minimize the deviations between model and data in performing a least squares fit. The number of model fit iterations had to be specified and additional model components were added and fitted in the same way. Once a good approximation to the data was found (which was checked by comparing the model visibilities to the data in the tasks RADPLOT, VPLOT,... as in the hybrid mapping process) a self-calibration of the phases was performed. It is always possible to reduce the deviations between a model and the data by adding more components, resulting in more degrees of freedom for the fitting procedure. For this, it had to be checked if the introduction of a new component improved the fit significantly to justify the necessity of this component. The quality of the achieved fit was determined by the value of χ^2, the likelihood, which is a measure of the deviations between model and data being the sum of the squared differences at each data point (in the visibility domain) divided by the number of degrees of freedom (reduced χ^2). For a good fit this value should be of the order of one.

The fits were performed initially independently in order not to be biased one by another. Once good fits for all four frequencies were obtained, a cross inspection of the resulting maps was done and the fits were modified in order to get a set of model fits as consistent as possible. Criteria for consistency are:

- Regions which show emission at two adjacent frequencies should be represented by the same number of components.
- In the outer parts components should tend to fade away towards higher frequencies as they most likely represent optically thin synchrotron emitting regions.

[2]Although less realistic than elliptical components, we used circular Gaussian components to reduce the degrees of freedom of the model and to make the models comparable between the different frequencies.

- In the inner parts of both jets there can be new components showing up at higher frequencies, which have no low frequency counterpart due to external or self absorption.

- Optically thin features should not show positional changes with frequency. In other words, it should be possible to align the model maps in a way that all optically thin features are connected by vertical lines, if the maps are plotted one above the other.

- Optically thick features are expected at the base of both jets and not at the outer parts. They should have the tendency to be shifted closer to the gap at higher frequencies exhibiting a "V"–like structure in the gap region.

- "Strange spectra", i.e. components which first become dimmer and then brighter again with rising frequency, indicate the influence of two distinct physical emission regions. They should be checked and possibly divided into two separate components.

To achieve a maximal consistency between adjacent frequencies, model components can be added to one of the two models if the reduced χ^2 decreases significantly. Alternatively, components can be taken away from the other model if this does not alter the value of χ^2 too much.

Tables 4.3 to 4.6 give the parameters of the final models for the four frequencies. The errors were determined with the program ERFIT, a program from the Caltech VLBI data analysis package (California Institute of Technology 1991), that calculates the statistical confidence intervalls of the fitted model parameters. The obtained values of χ^2 are all satisfactory small but at the price of a rather big number of model components. Over the frequencies 15 model components were needed for the eastern jet of which 9 are contained in the 5 GHz–fit and 11, 8 and 10 in the 8.4, 22 and 43 GHz–fits, respectively. For the western jet 4, 6, 5 and 3 components were needed for the fits resulting to a total number of 8 jet components after the cross identification. Especially the cross check of the resulting maps with the total intensity maps obtained with the CLEAN algorithm argued convincingly against a smaller number of components at any frequency. The image alignment was performed in three steps:

1. A reliable alignment of the model fit maps had to be found. For this the fitted components first had to be cross–identified. Then the model fit maps could be aligned pairwise, assuming frequency independent positions of optically thin features. Above 8.4 GHz the position of the component A7 in the 43 GHz model was used as a measure of relative shifts between adjacent frequency models since this component is relatively strong at all three frequencies and unambiguously identifyable. A shift of 0.008 mas to the west and 0.014 mas to the south of the 22 GHz model as well as of the 8.4 GHz model (with respect to the 43 GHz model) was determined. For the alignment of the 5 GHz and the 8.4 GHz model fit maps the distance between the two most distant components was measured and the center was calculated for both frequencies. This center then was assumed to be intrinsically spatially coincident resulting to a shift of 0.115 mas to the west and 0.051 mas to the south for the 5 GHz model.

   In Figure 4.3 the aligned model fit maps are shown and the model fit component identifications are indicated by lines. The most distant component in the eastern jet was labeled as A1, the adjacent inner one as A2, and so on. The western jet was devided into three parts following the convention introduced in Section 4.1 . The model fit component in the innermost part of the western jet were labeled as B2b, B2a, B1 from east to west. Further out the components C3b, C3a, C2, C1 and D follow.

Most of the lines in Figure 4.3 are nearly vertical indicating frequency independent component positions. This fact underlines the reliability of the obtained fits as a high quality approximation of the true source structure strikingly. Inclined connection lines arise only at points where components split into two distinct ones at the higher frequency whereas the data set could be modelled as well with only one component at the lower frequency.

At the inner edge of the eastern jet new components are showing up at higher frequencies as the innermost region components of the western jet do between 5 and 8.4 GHz. Above 8.4 GHz the innermost component in the western jet B2b moves slightly to the east. These effects represent the core–shift, discussed in detail in Section 4.6 .

2. In order to align the CLEAN maps their charactristic features first had to be identified with model components in the corresponding "model fit map". These CLEAN map features were set at the relative position of the cross–identified model components. For this the brightness peak of region C was identified with C3 in the 5 and 8.4 GHz maps, and component B2b was ascribed to the brightness peak of region B for the other pairs of CLEAN maps. The aligned CLEAN maps are shown in Figure 4.4. They contain the whole multi-frequency information obtained in the observation and will be used in the next section to derive the spectral index distribution across the source.

3. A fixpoint can be determined from which angular distances are measured as absolute distances rather than relative distances between distinct components. A natural choice for this fixpoint would be the most probable position of the true center of jet activity, namely the position of the central engine. The center between the components A15 and B2b was chosen for this purpose (see Section 4.6). The component positions in Table 4.3 to 4.6 are given relative to this reference point.

In Figure 4.2 the locations of the model components in the sky at all four observed frequencies are shown. The cross–identification of the various components is very obvious in this plot for the most cases. The errors in x (R.A.) and y (Dec.) have been calculated from the statistical errors in r and ϕ, from the ERFIT-output. For the most components, these errors are to small to be visible in Figure 4.2, especially at the highest frequencies. The components in both jets do not follow a straight trajectory, but are aligned along a helical path. The helical structure is more pronounced at the highest frequencies and has an opening angle of $\sim 10^\circ$ in the eastern jet and $\sim 15^\circ$ in the western jet.

Although the pieces of this puzzle fit convincingly well, it has to be remarked that the method of alignment used here is not *a–priori* definite. It is based on the assumption that optically thin components have frequency-independent positions and that the cross identification of the model components is correct. However, it is obvious that the used identification is the most reasonable as a shift of the whole set of model components

Table 4.3: 5 GHz model fit parameters ($\chi^2_{red} = 1.12$).

Component	Flux density [mJy]	Radius[a] [mas]	P.A.	FWHM [mas]
A1	80±2	14.56±0.03	66.5±0.1	2.14±0.03
A2	54±2	12.01±0.04	63.6±0.1	1.87±0.08
A3	60±2	9.61±0.05	65.3±0.3	1.63±0.04
A4	150±7	7.46±0.05	71.7±0.2	0.99±0.02
A5	338±37	6.0±0.2	72.8±0.1	0.93±0.25
A6	447±48	5.1±0.1	72.8±0.2	0.83±0.19
A7/8	450±28	4.0±0.1	71.0±0.2	0.69±0.08
A9	397±30	3.1±0.2	71.1±0.3	0.20±0.07
A10	140±37	2.3±0.2	70.9±0.4	0.46±0.05
C3	137±3	3.84±0.03	-114.2±0.1	1.03±0.06
C2	59±3	4.75±0.06	-115.7±0.3	0.83±0.09
C1	24±1	7.19±0.03	-119.6±0.4	1.85±0.10
D	67±1	11.81±0.01	-114.7±0.1	2.24±0.05

[a] The radius is measured from the center between A15 and B2b (see Section 4.6).

Table 4.4: 8.4 GHz model fit parameters ($\chi^2_{red} = 1.76$).

Component	Flux density [mJy]	Radius[a] [mas]	P.A.	FWHM [mas]
A1	38±1	14.70±0.03	66.5±0.1	2.00±0.03
A2	37±1	12.04±0.04	64.0±0.1	2.34±0.08
A3	36±1	9.30±0.05	65.9±0.3	1.62±0.04
A4	83±4	7.34±0.05	71.9±0.2	0.98±0.02
A5	72±8	6.4±0.2	72.7±0.1	0.59±0.25
A6	360±26	5.5±0.1	72.8±0.2	0.81±0.12
A7	396±22	4.4±0.1	72.3±0.2	0.74±0.06
A8	146±8	3.8±0.1	69.7±0.2	0.28±0.06
A9	360±21	3.2±0.2	71.3±0.3	0.34±0.05
A10	316±47	2.7±0.2	69.2±0.4	0.31±0.03
A11	137±25	1.9±0.2	74.3±0.4	0.34±0.07
B2a/b	56±4	0.60±0.03	-119.8±0.1	0.36±0.02
B1	29±2	1.26±0.03	-119.9±0.1	0.31±0.02
C3	20±1	3.75±0.03	-114.2±0.1	1.06±0.08
C2	77±4	4.86±0.06	-114.9±0.3	0.90±0.09
C1	21±1	7.03±0.03	-119.1±0.4	1.68±0.10
D	48±1	11.95±0.01	-114.7±0.1	2.21±0.05

[a] The radius is measured from the center between A15 and B2b (see Section 4.6).

Table 4.5: 22 GHz model fit parameters ($\chi^2_{red} = 0.71$).

Component	Flux density [mJy]	Radius[a] [mas]	P.A.	FWHM [mas]
A6	138±5	5.48±0.03	72.4±0.2	0.98±0.04
A7	140±7	4.39±0.01	72.2±0.2	0.65±0.03
A8	99±5	3.72±0.01	68.1±0.2	0.47±0.03
A9	139±6	3.09±0.01	72.2±0.2	0.32±0.02
A10	144±5	2.70±0.01	68.5±0.2	0.27±0.01
A11	44±8	1.98±0.04	73.0±0.8	0.29±0.07
A12	86±15	1.53±0.04	72.1±0.4	0.26±0.06
A13	54±14	1.20±0.04	71.1±0.9	0.22±0.06
B2b	341±14	0.52±0.02	-123±1	0.21±0.01
B2a	151±14	0.72±0.05	-115±2	0.29±0.02
B1	31±2	1.38±0.02	-132±1	0.3±1.7
C3a	50±4	3.34±0.02	-116.4±0.4	0.58±0.03
C3b	86±6	4.18±0.07	-116±1	1.95±0.16

[a] The radius is measured from the center between A15 and B2b (see Section 4.6).

Table 4.6: 43 GHz model fit parameters ($\chi^2_{red} = 0.83$).

Component	Flux density [mJy]	Radius[a] [mas]	P.A.	FWHM [mas]
A6	40±2	5.36±0.03	72.8±0.2	0.92±0.05
A7	44±2	4.39±0.01	72.2±0.2	0.51±0.03
A8	39±2	3.76±0.01	68.7±0.1	0.46±0.03
A9	37±1	3.177±0.003	71.8±0.1	0.22±0.01
A10	70±1	2.772±0.004	68.4±0.1	0.33±0.01
A11	19±1	1.95±0.01	71.6±0.5	0.32±0.03
A12	57±2	1.499±0.004	70.2±0.2	0.22±0.01
A13	43±2	1.221±0.006	70.8±0.2	0.12±0.01
A14	54±1	1.017±0.003	71.9±0.2	0.08±0.05
A15	19±1	0.47±0.01	61±2	0.21±0.03
B2b	225±2	0.467±0.002	-119.2±0.3	0.224±0.002
B2a	31±2	0.779±0.007	-120.9±0.6	0.22±0.01
C3b	27±2	3.33±0.05	-116.5±0.8	0.95±0.08

[a] The radius is measured from the center between A15 and B2b (see Section 4.6).

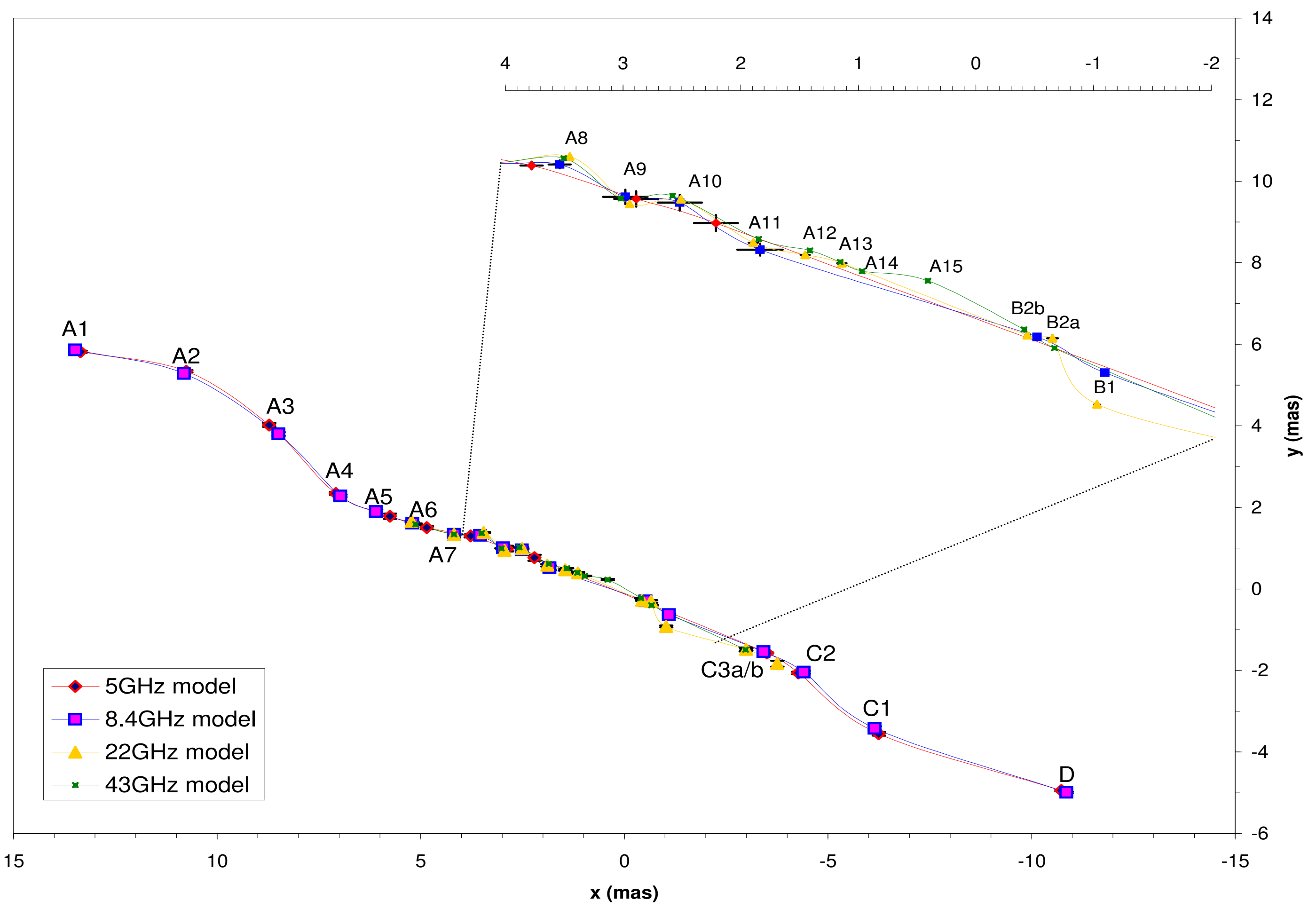

Figure 4.2: Locations of the various model components at all four observed frequencies on the sky. The positional errors in x and y have been calculated from the statistical errors in r and ϕ, as given by the ERFIT-output and are indicated in the inlaid magnification of the inner 6 mas of the source structure. The model components are aligned along a helical path with an opening angle of $\sim 10°$ of the eastern jet and $\sim 15°$ of the western jet.

concatenated with another identification introduces physical implausibilities. If one, for example, identifies the outermost component in the 8.4 GHz map with the second (counted from the east) component at 5 GHz, many of the components in the western jet have no direct counterpart and component D must be interpreted as an optically thick feature below 8.4 GHz, which seems very unlikely (see Figure 4.3). However, all possible combinations of other identifications have been tested but dismissed because of such physical implausibilities.

An impression of the full multi-frequency structure of NGC 1052 can be obtained from a film produced from the maps at the four observing frequencies. Two versions are available (see Appendix D for a detailed description), which can be obtained via the Internet at the URLs: `http://www.mpifr-bonn.mpg.de/staff/mkadler/hollywood_1052.avi` and `http://www.mpifr-bonn.mpg.de/staff/mkadler/ufa_1052.avi`, respectively.

4.3 Spectral analysis

After obtaining a reliable registration of the four maps of NGC 1052 and a cross–identification of the model fit components, there are two approaches to study its spectral properties. The first approach is to use the knowlwdge of the proper alignment of the CLEAN maps to derive maps of the spectral index between two adjacent frequencies. The second one is to derive spectra of the model fit components. Both approaches are somewhat complementary. The latter gives a handy number of component spectra which can be analyzed in detail, whereas the spectral index mapping represents the course of the spectral index along the jet axis in a more complete way yielding additional information at parts of the jet which are not represented by model components. The results of both approaches will be presented in this section.

Spectral index mapping In order to compare the aligned CLEAN maps at adjacent frequencies directly, special renditions are needed with matching uv–ranges and a common restoring beam. This can be achieved using the commands *uvtaper* and/or *restore* at the beginning and the end, respectively, of the hybrid mapping process in DIFMAP. Table 4.7 gives the restoring beams and the other relevant parameters of the derived maps. After being aligned, using the method described in the previous section, they were read into $\mathcal{AIPS}$ and combined to a spectral index map[3] using the task COMB. Since the spectral index can only be calculated meaningful at pixels above the 1σ noise level, information

[3]At each pair of pixels of the two (coinciding) maps, the spectral index α is calculated from the flux densities per beam S_1 and S_2 at the two frequencies ν_1 and ν_2: $\alpha = (\lg S_1 - \lg S_2)/(\lg \nu_1 - \lg \nu_2)$

Table 4.7: Spectral index map parameters

ν_1 [Hz]	ν_2 [Hz]	Common Beam [mas × mas, °]	Lowest Contour$_1^a$ (mJy/beam)	Lowest Contour$_2^b$ (mJy/beam)	*Contours*$_3^c$ [(mJy/beam) × (levels)]
5	8.4	2.64 × 1.06, -3.805	2	2	(-2.5,-1.5,-0.5,0,0.5,1.5,2.5)
8.4	22	1.42 × 0.565, -5.75	1	1	(-2.5,-1.5,-0.5,0,0.5,1.5,2.5)
22	43	0.655 × 0.240, -7.78	1	1	(-2.5,-1.5,-0.5,0,0.5,1.5,2.5)

[a] Lowest contour in the low–ν map; [b] Lowest contour in the high–ν map; [c] Contours in the spectral index map.

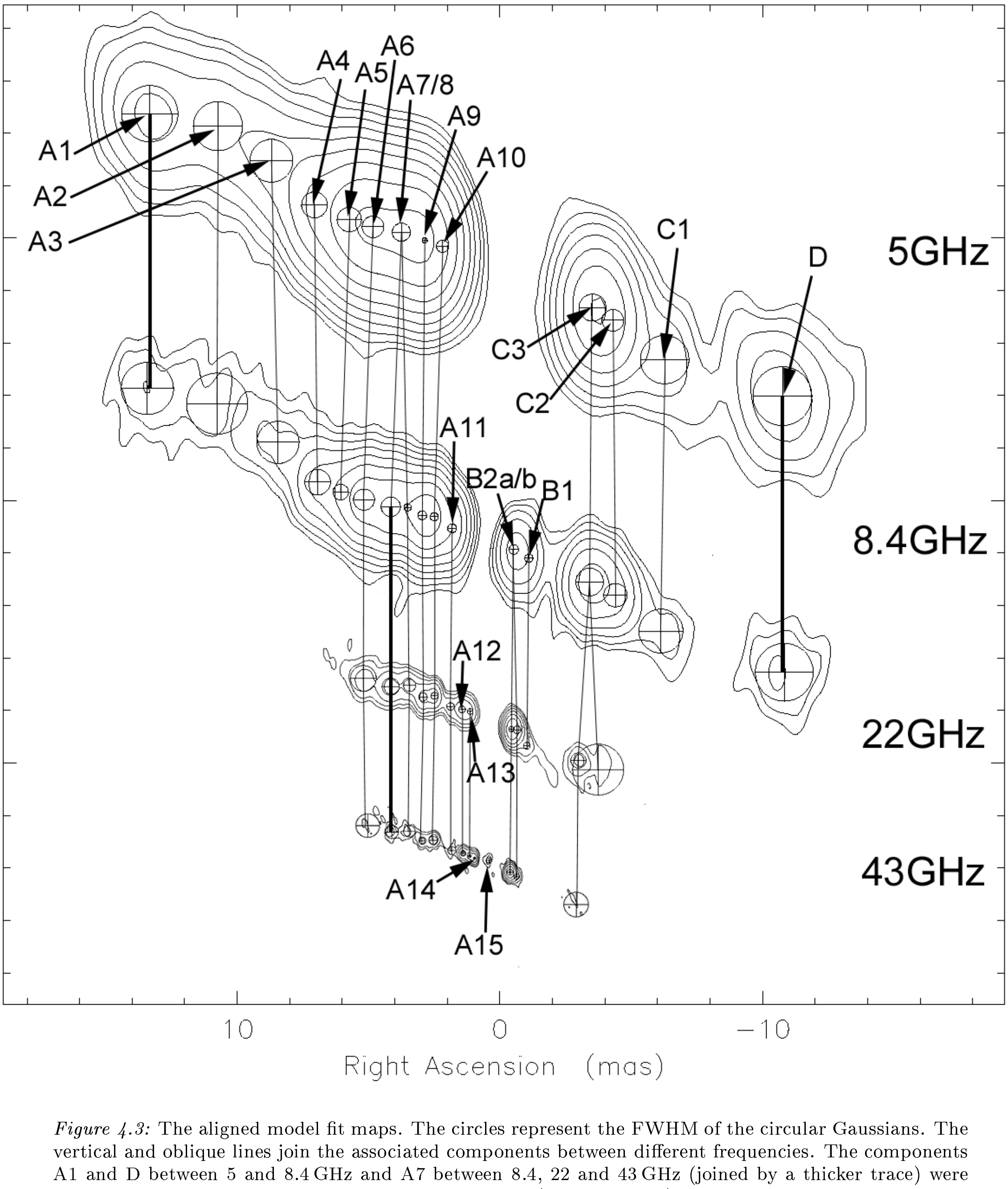

Figure 4.3: The aligned model fit maps. The circles represent the FWHM of the circular Gaussians. The vertical and oblique lines join the associated components between different frequencies. The components A1 and D between 5 and 8.4 GHz and A7 between 8.4, 22 and 43 GHz (joined by a thicker trace) were used for the alignment. The contours are 1.872 mJy × (-1,1,2,4,...,256) for the 5 GHz model, 2.62 mJy × (-1,1,2,4,...,128) for the 8.4 GHz model, 5.01 mJy × (-1,1,2,4,...,64) for the 22 GHz model and 3.45 mJy × (-1,1,2,4,...,32) for the 43 GHz model. The beams are 3.08 × 1.29 mas at 0.851° at 5 GHz, 1.95 × 0.806 mas at -3.97° at 8.4 GHz, 0.75 × 0.325 mas at -1.32° at 22 GHz and 0.385 × 0.161 mas at -2.62° at 43 GHz,

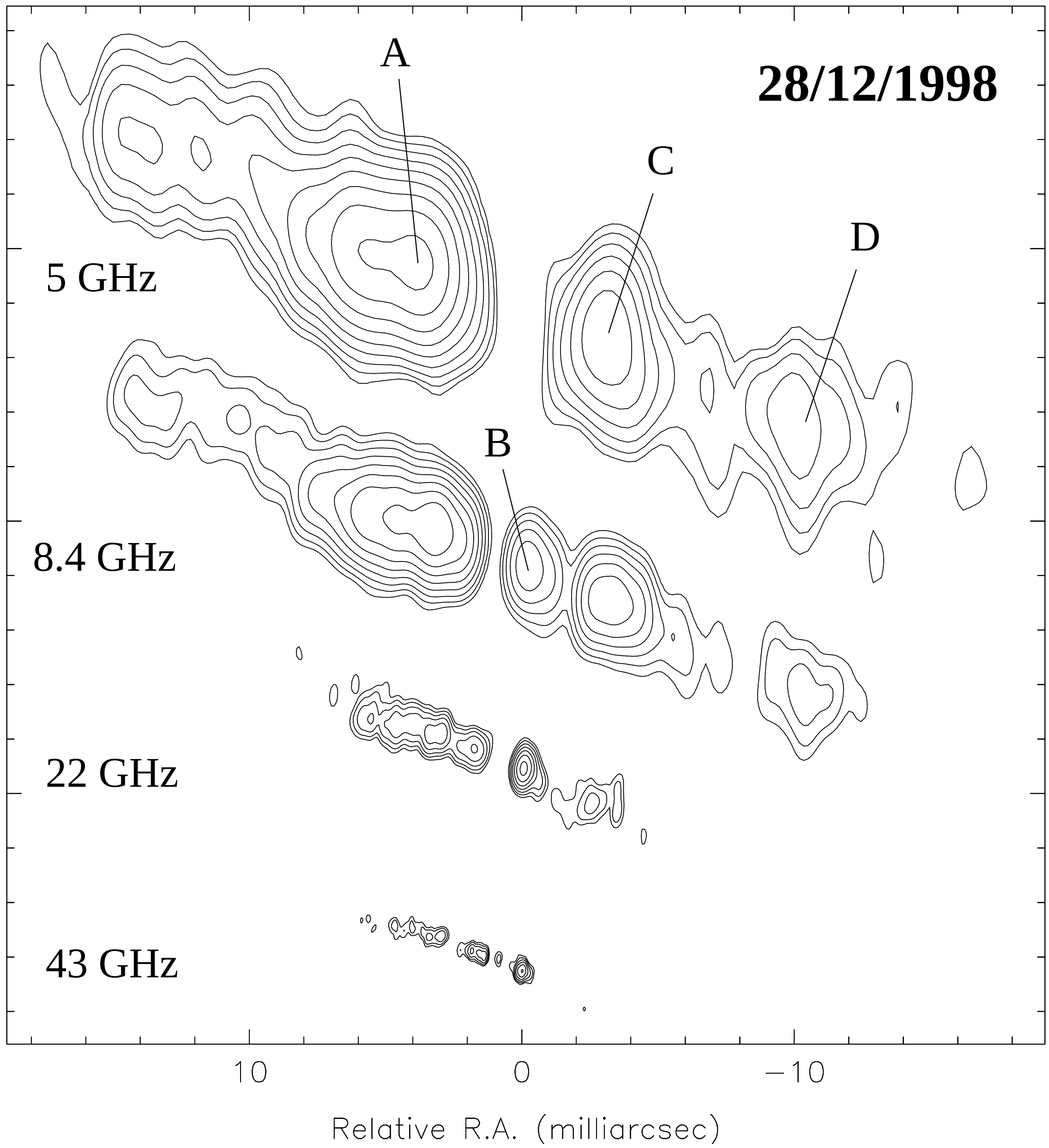

Figure 4.4: The aligned CLEAN maps. The contours are as given in Table 4.2, but without the two lowest contour levels. The beamsizes are the same as in Figure 4.1.

below 1 mJy/beam was discarded. This flux density threshold can introduce artifical features at the edges of the resulting spectral index map, which should not be interpreted as intrinsic source features.

A common slice through the spectral index maps was chosen (P.A. = 69.3°) to give a profile of the spectral index behaviour. This choice is in good agreement with the jet–axis at the inner part but a little too large in the outer part because of the curved jet structure. In order to avoid this it would be necessary to define a series of slice segments along the ridge line of the source. Nevertheless, the slice matches the jet axis at 5 GHz quite well and an examination of the spectral index maps shows that there are no unphysical trends visible, perpendicular to the slice. For this, the mismatching of the jet axis in the outer parts of the jet seems tolerable. The common–beam maps are shown pairwise in Fig 4.5 to 4.7 together with the spectral index maps. Additionally the figures show the course of the flux density and the value of the spectral index, respectively, along the slice. The latter were determined using the task SLICE in $\mathcal{AIPS}$.

The main feature in each spectral index map is an optically thick inner edge of the innermost part of both jets. Outwards, the spectral index tends to decrease but is superimposed by local extrema. Some of these are actually a composite of several blended lines making it difficult to judge the overall quality of the registration just by looking at the brightness cuts. Nevertheless, the inconsistencies in position are small and can be estimated to be of the order of ±1 map pixel (corresponding to 0.3,0.15 and 0.075 mas in the 5-8.4, 8.4-22 and 22-43 GHz map, respectively).

Between 5 GHz and 8.4 GHz the spectral index α diverges at the region of the components A11 and B2[4] (see Figure 4.5). The value of 2.5 is exceeded on both sides indicating a region of extrinsic absorption at the center of NGC 1052. The spectral index at the inner edge of the eastern jet, however, is affected by the tail of the B2 component which contributes to this region at 8.4 GHz due to the size of the beam. The position where this effect is negligible is indicated by the first kink in the eastern part of the spectral index slice around map pixel 120. At this point the spectral index is still above the theoretical maximum of 2.5 for self absorption but a small shift of the 5 GHz map to the east would probably drop it to values around 1. In the outer part of the eastern jet the spectral index oscillates around ~ -1, therefore being optically thin. The western jet also shows a decrease of the spectral index from ~ 2 at the region of C3 and C2 to ~ 1 around D.

Between 8.4 and 22 GHz (Figure 4.6) the spectral index in the eastern jet is extremely smooth between the regions of A5 and A11, followed by a very sharp rise towards A12 and A13 with values of α up to 3.5. On the western side there are also very high values of α but not larger than 2.5, not ruling out the possibility of external absorption but being compatible with internal self absorption of the jet core. Outwards in the western jet, there is a kink in the decrease of α which is again an artificial contribution of the optically thick components of the other jet side (A12 and A13), which tails are folded partially onto the western side. Behind this kink the spectral index keeps falling until it rises again very quickly at the inner edge of the region C. On the outer part of the C region α falls down below values of -1.

Between 22 and 43 GHz (Figure 4.7) the spectral index is fairly constant with values around -1.5 on the eastern side and a rise up to $+1.5$ from the region of the component

[4]In this section the components A1 to D serve just as a way to describe a special region in the source. "The region around C", e.g. means the part of the western jet between 2 and 8 mas from the gap.

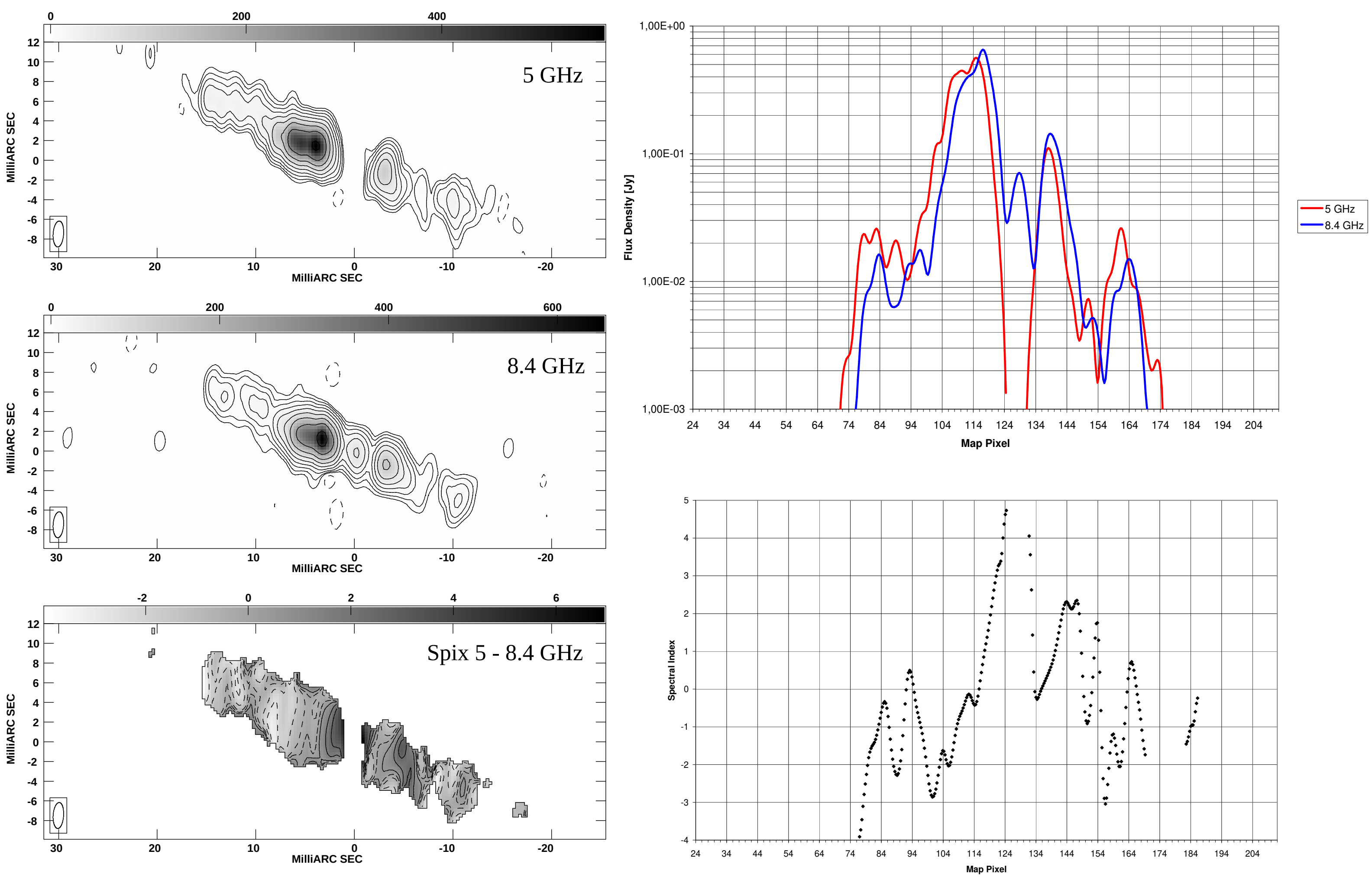

Figure 4.5: Left hand side: Total intensity maps of NGC 1052 at 5 GHz and 8.4 GHz (top) restored with a common beam and the spectral index map between 5 and 8.4 GHz (bottom). The contours and beam parameters are given in Table 4.7. Right hand side: The course of the brightness (top) and the spectral index (bottom) along a P.A. of 69.3° (top left corner to bottom right cornor of the images on the left side.

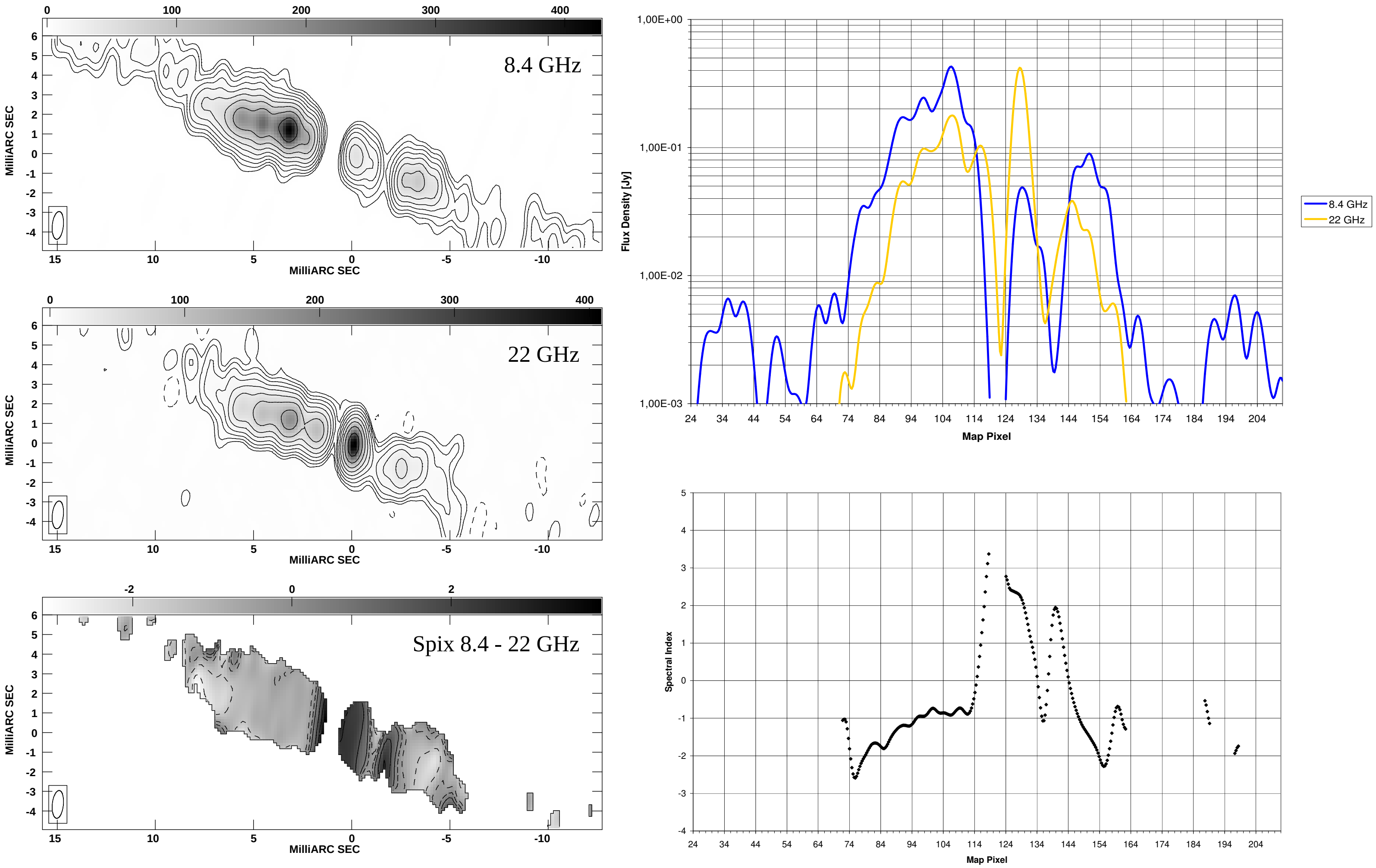

Figure 4.6: Left hand side: Total intensity maps of NGC 1052 at 8.4 and 22 GHz (top) restored with a common beam and the spectral index map between 8.4 and 22 GHz (bottom). The contours and beam parameters are given in Table 4.7. Right hand side: The course of the brightness (top) and the spectral index (bottom) along a P.A. of 69.3° (top left corner to bottom right cornor of the images on the left side.

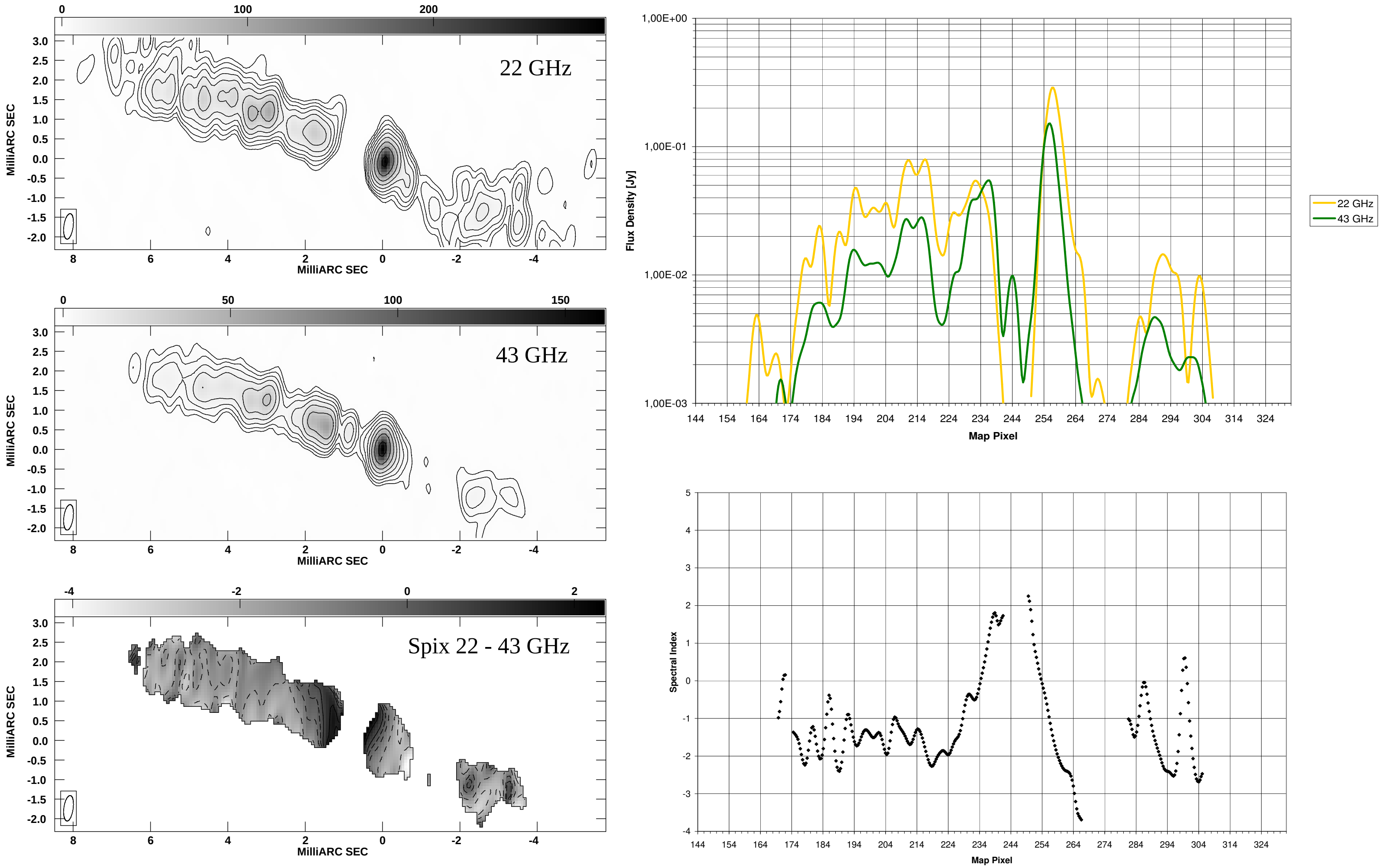

Figure 4.7: Left hand side: Total intensity maps of NGC 1052 at 22 and 43 GHz (top) restored with a common beam and the spectral index map between 22 and 43 GHz (bottom). The contours and beam parameters are given in Table 4.7. Right hand side: The course of the brightness (top) and the spectral index (bottom) along a P.A. of 69.3° (top left corner to bottom right cornor of the images on the left side.

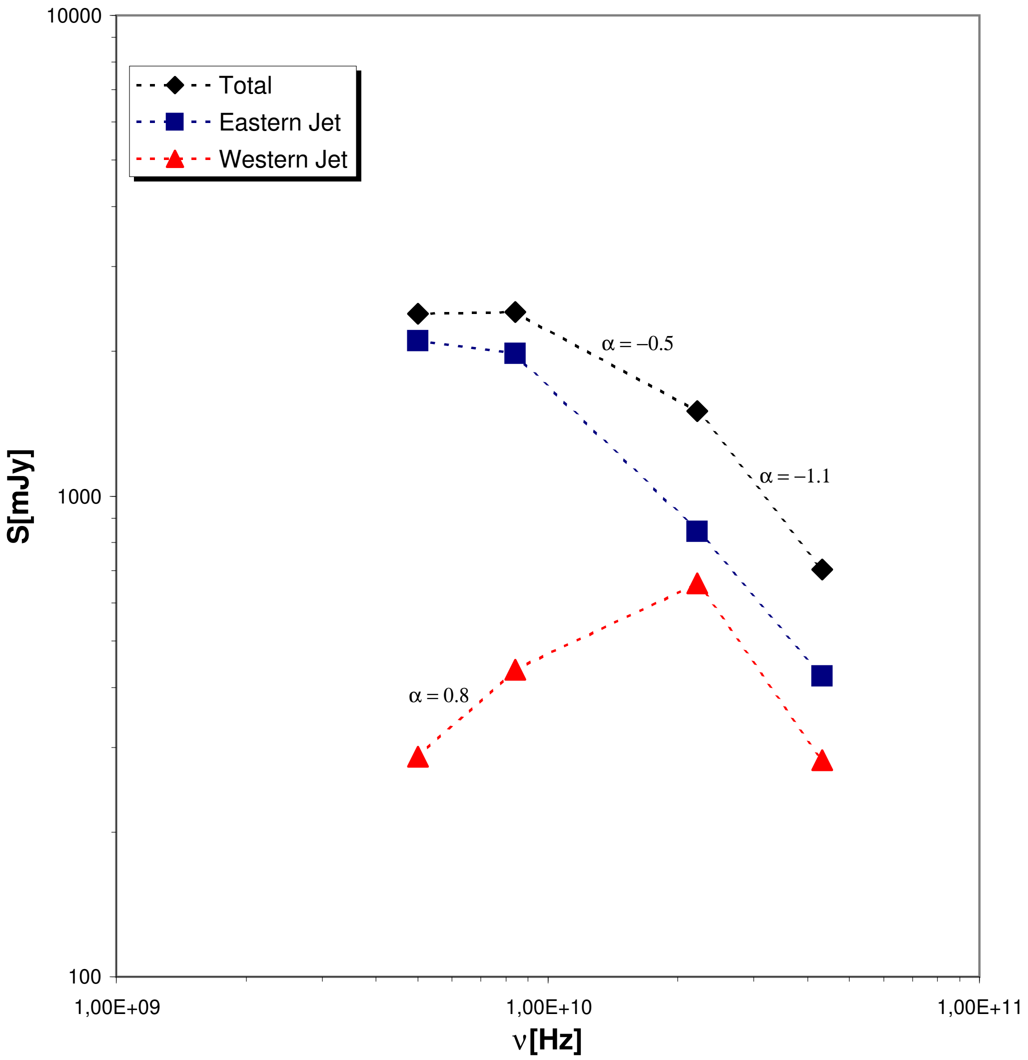

Figure 4.8: Total spectrum of the pc-scale structure of NGC 1052 (as imaged with VLBI) and the two jet spectra between 5 and 43 GHz. No errors are given, since these are negligible small.

A12 inwards. On the western side α rises from the outer edge of component B to its inner edge from values below -2 approaching 2.5 but not exceeding it. In the region around component C the spectral index falls from -1 to -2.5 going outwards with two peaks inbetween.

The influence of external absorption on the the western jet is undisputable since no counterpart of the B2 component is present at 5 GHz. The structure of the eastern jet is rather continuous with no strong and isolated components at its inner part. The data however, indicate a region of external absorption, comparable in extend to the western side. In sum, there are hints for the presence of an obscuring torus or thick disk from the analysis of the spectral index maps, which covers the core of the western jet but also a substantial fraction of the inner eastern jet.

Spectral analysis of the model fit components The flux densities of the model fit components in Table 4.3 to 4.6 can be used to derive spectra of 1) the whole pc-scale structure, 2) the two jets separately and 3) the model fit components themselves. In Figure 4.8 the total spectrum of the pc-scale structure of NGC 1052 between 5 and 43 GHz is shown as well as the spectra of both jets separately. All values were obtained by adding up flux densities[5] of model components (A1 to A15 for the eastern jet and B2b to D for the western one). Components that are not found at a special frequency were given the flux density zero.

At the high frequencies both jets show similar spectra with an optically thin decrease of the flux density above 22 GHz. The spectral index in this regime is around -1 in both jets, with the eastern jet being significantly stronger than the western one. This implies that the eastern jet is the approaching one whereas the western jet is the counterjet. However, below 22 GHz the behaviour of the two spectra differs substantially. The eastern jet spectrum remains optically thin above 8.4 GHz and turns over around 5 GHz. The western jet, on the other hand exhibits a sharp cut–off in its spectrum below 22 GHz with the spectrum becoming even more inverted below 8.4 GHz. Although the spectral index is not above 2.5 the possibility of synchrotron self-absorption seems very unlikely to be responsible for the turnover of the spectrum because of two reasons. First, the similarity of the spectra of eastern and western jet at high frequencies proposes similar intrinsic physical properties on both sides making it suspicious that the self absorption frequency differs by at least a factor of 3. Second, the kinematical analysis of Vermeulen et al. (2002) shows the jet axis to be close to the plane of the sky and the motions to be only weakly relativistic. There is little evidence for strong Doppler boosting. Moreover, such an effect should shift the turnover frequency of the counterjet to lower frequencies, rather than to higher ones.

If the spectrum of the western jet is decomposed into the spectra of the different jet regions A, B, C and D (see Figure 4.9) it turns out, that the region B, the innermost region on the western side, is responsible for the cut–off of the western jet spectrum below 22 GHz. Its spectrum between 8.4 and 22 GHz is highly inverted with a spectral index of 1.9 but the fact that it is not detectable at all at 5 GHz makes the spectral index in this regime larger than 4. Such big positive spectral indices cannot be due to synchrotron self absorption but indicate a region of external absorption in front of the source. The spatially isolated position of this component rules out arguments dealing with misregistration effects and makes this case one of the most pronounced external absorption effect in extragalactic radio sources. The highly inverted spectrum of this component in NGC 1052 and the necessity of an external absorber was first mentioned by Kellermann et al. (1999) and later confirmed by Kameno et al. (2001). Other sources in which evidence for an central free-free absorber was found are e.g., Cen A (Tingay & Murphy 2001), NGC 1275 (Vermeulen et al. 1994), NGC 4261 (Jones et al. 2000) and 0108+388 (Marr et al. 2000).

One open question at this point is, whether the eastern jet is also affected by external absorption or not. Kameno et al. proposed an obscuring torus, covering 0.7 mas of the western jet and 0.1 mas of the eastern jet. However, their results are very sensitive to shifts in the registration of the multi-frequency maps. Figure 4.10 shows the spectra of the model fit components of the eastern jet. Most components show optically thin synchrotron spectra with spectral indices around -1. The outer components A1, A2, A3, A4 and A5 show typically optically thin spectra and become too dim to be detected at

[5]For all quantities that are derived from the model component flux densities, a standard error calculation has been performed. The calculated errors are indicated in the plots, where they are not negligible.

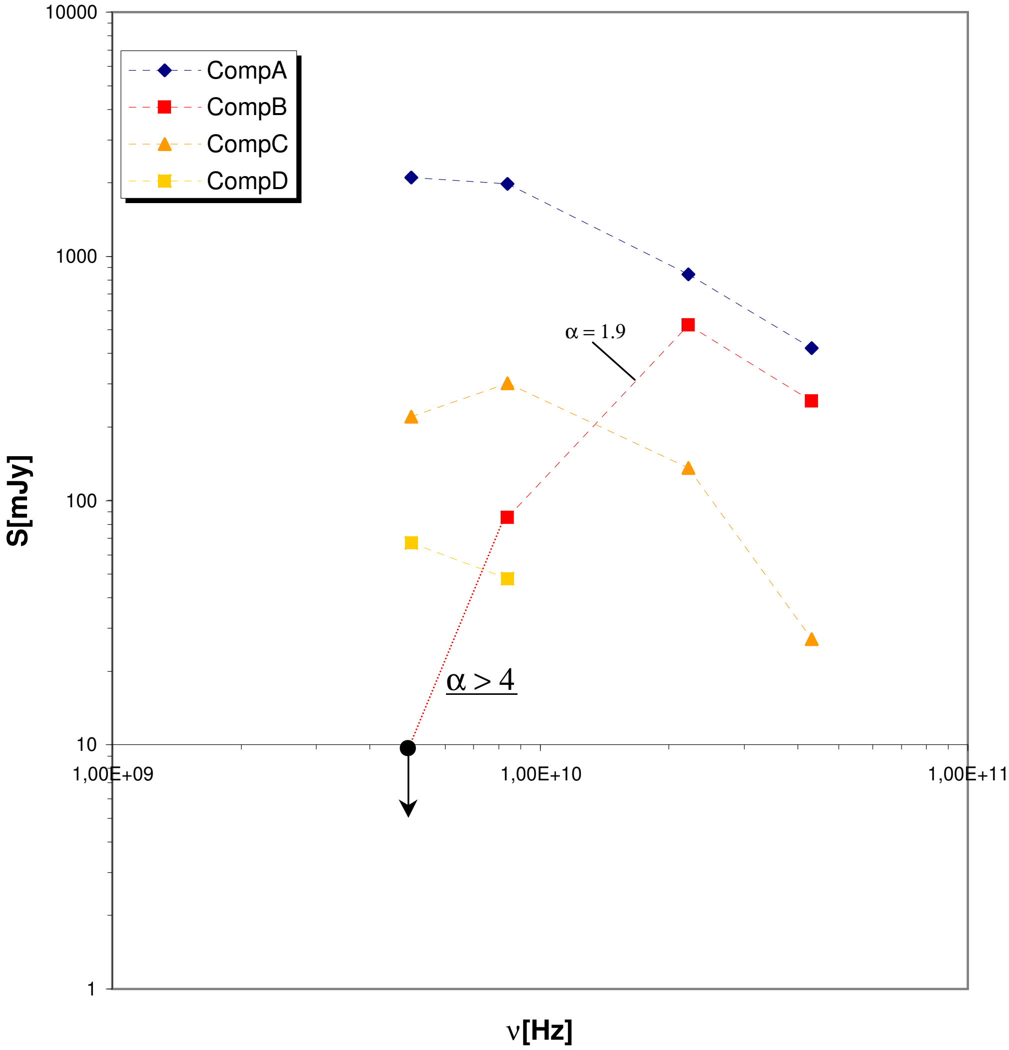

Figure 4.9: The spectra of the four jet regions A,B,C and D (see Figure 4.1 for the definition of the jet regions). No errors are given, since these are negligible small.

frequencies above 8.4 GHz. The very flat spectral index of some spectra (e.g. A6, A9) below 8.4 GHz indicates a turnover of the spectrum around 5 GHz. There is a general trend of the turnover of the components spectra to be shifted to lower frequencies the farther from the core a component is located. A12 and A13, e.g. are (self-) absorbed at low frequencies and seem to have their turnover close to 43 GHz.

The A11 counterpart is not detected at 5 GHz. Estimating (conservatively) a flux density of 10 mJy at 5 GHz yields a spectral index of 5. This would suggest that the innermost part of the eastern jet is also strongly affected by external absorption. However, the A10 and A11 components are very close to each other. If both flux densities are summed up at 5 and 8.4 GHz, a spectral index of 2.3 can be calculated, a value very close to the expected one for pure synchrotron self-absorption. Due to the small distances between the inner components in the eastern jet it cannot finally be judged, whether free-free absorption plays an important role or not. In Figure 4.11 the formal spectral indices of the components in the eastern jet are shown as a function of distance along the jet.

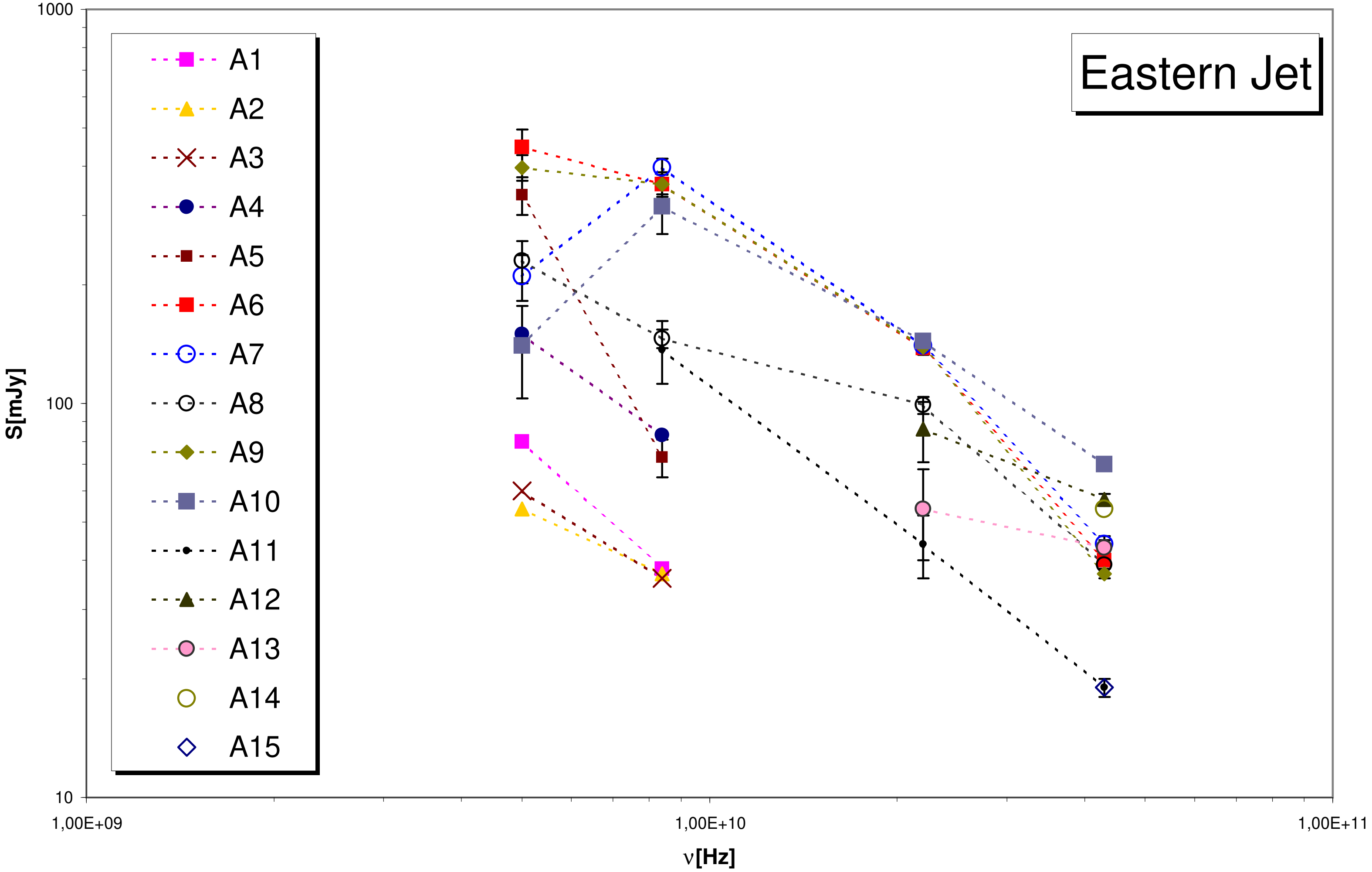

Figure 4.10: Spectra of the model fit components in the eastern jet (see Figure 4.3 for the locations of the various components). Errorbars for the components A5 to A13 are given. For the remaining components the errors are negligible.

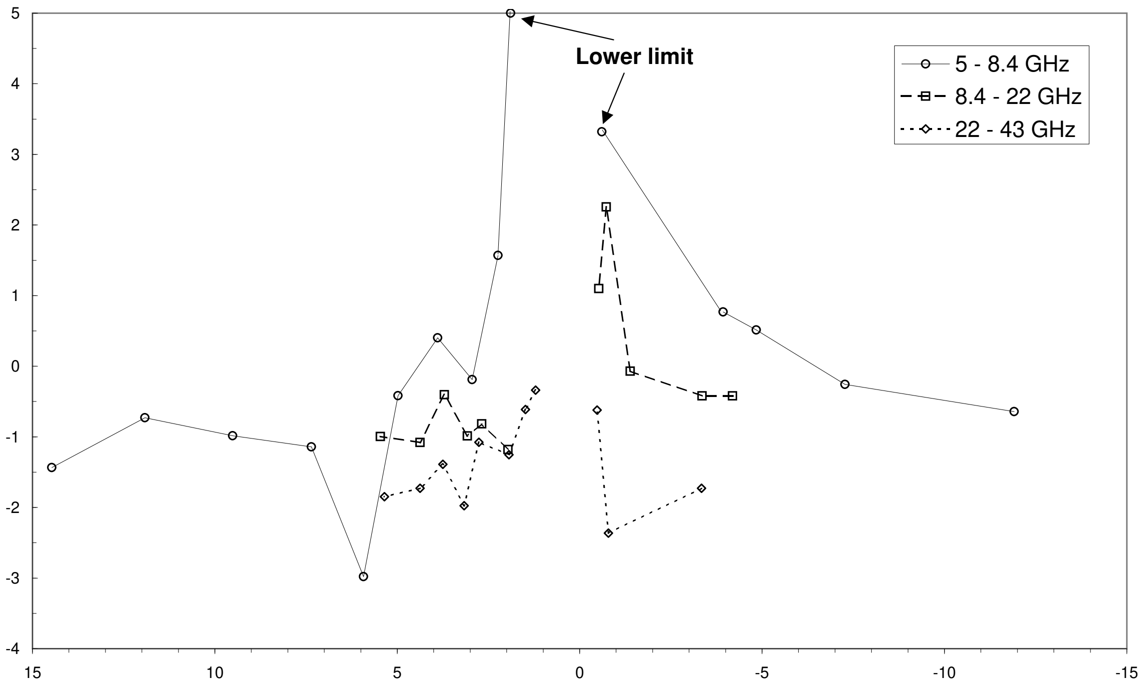

Figure 4.11: The spectral indices of the model components between 5 and 8.4 GHz, 8.4 and 22 GHz, as well as between 22 and 43 GHz (compare to Figure 4.5 to 4.7). Lower limits for the spectral indices between 5 and 8.4 GHz of the two innermost components at 8.4 GHz (B2a/b and A11), calculated from an upper limit of 10 mJy flux density at 5 GHz, are shown.

Their errors have been calculated from the formal errors of the model components, using a standard error calculation. A comparison with Figure 4.5 to 4.7 gives a good qualitative agreement to the slices through the spectral index maps of NGC 1052.

From the model fitted flux densities of both jets the jet-to-counterjet ratio of NGC 1052 can be determined. Figure 4.12 shows the ratio of the flux densities of the model components on either side of the gap as a function of frequency. At 5 GHz the eastern jet outshines the western one by a factor of 7.34. At 8.4 GHz it is still brighter than the counterjet by a factor of 4.56 but falls close to unity at 22 GHz. At 43 GHz the ratio rises again to 1.5. This behaviour is quite untypicall as in other similar sources (e.g. in Cygnus A) the ratio at 5 GHz is rather small increasing towards higher frequencies and reaching a maximum, before it finally falls again. The maximum is usually explained by resolution effects of the central absorber. At low frequencies the obscured area of the counterjet is unresolved so the obscuration has no net impact on the intrinsically frequency-independent jet-to-counterjet ratio. With rising frequency the obscuration has a bigger influence, as the resolution increases and the obscured area becomes resolved. At even higher frequencies the frequency dependence of free-free absorption makes the absorber partially transparent and the jet-to-counterjet ratio falls back to its initial value (which may differ from unity, due to boosting effects). This picture can explain the rise (or at least the stopped decrease) of R above 22 GHz, implying that the absorber covers a large fraction of the counterjet at 5 GHz. This is no surprise since component B is totally absorbed at 5 GHz. More surprising is the fact that the jet-to-counterjet even keeps rising at lower frequencies up to 50 at 2.3 GHz (Kameno et al. 2001). This suggests that either a much bigger part of the western jet is covered by the absorber or that curvature effects

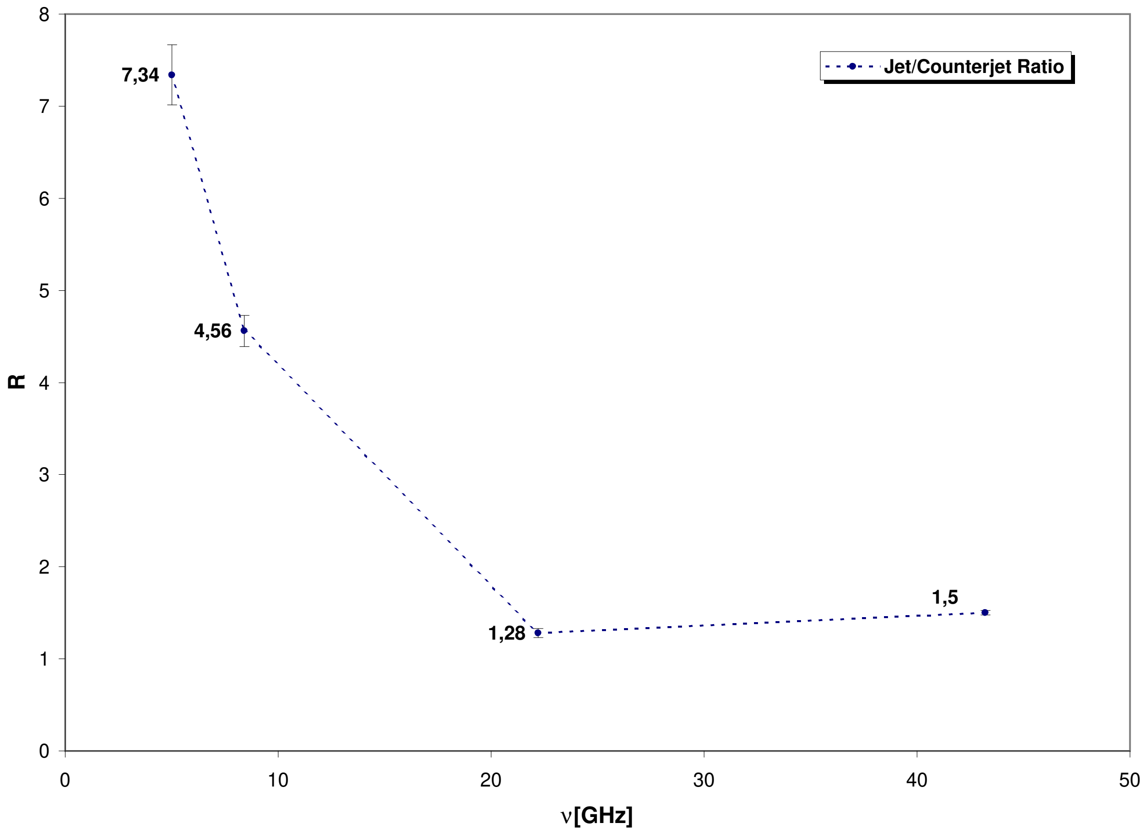

Figure 4.12: The jet-to-counterjet ratio determined from the fluxes of the model fit components as a function of frequency

play an important role. In the first scenario the density of the absorber falls fast enough with radius that at 5 GHz the absorber has become optically thin a few milliarcseconds from the core and component C is only weakly absorbed. In the latter case, the counterjet bends away from the observer at a distance of a few milliarcseconds from the core and its radiation is Doppler de–boosted.

4.4 Brightness temperature distribution

In this section a method of analyzing the brightness temperature distribution along a jet is presented and applied to the eastern jet of NGC 1052. This method provides a tool to find regions in a jet which are affected by external absorption. In the inner region of the eastern jet of NGC 1052 this method unveils the existence of an obscuring torus and sets limits to its geometrical extent and density.

The brightness temperature of a source is defined as the temperature of a blackbody, producing the same flux density at the measured frequency as the source. For a non-thermal source the brightness temperature is a frequency-dependent quantity. From this definition follows (see e.g. Condon et al. 1982)

$$T_b = \frac{1}{\pi r^2}\frac{c^2 S_\nu}{2k_B\nu^2} = 1.22\cdot 10^{12}\mathrm{K}\left(\frac{S_\nu}{\mathrm{Jy}}\right)\left(\frac{\nu}{\mathrm{GHz}}\right)^{-2}\left(\frac{\Theta}{\mathrm{mas}}\right)^{-2} \tag{4.1}$$

with S_ν the flux density of the source, ν the observing frequency, r the diameter of the source and Θ its apparent diameter at half maximum[6]. According to this equation, brightness temperatures have been computed for the model fit components at all four frequencies. The resulting values are given in Table 4.8 to 4.11. The uncertainties in T_b were computed using Gaussian error propagation from the errors in flux density and FWHM of the model components (see Table 4.3 to 4.6). In Figure 4.13 the brightness temperatures of the eastern jet are plotted as a function of distance from the central engine. Once again, this was assumed to lie at the center between the components A15 and B2b (see Section 4.6 for a detailed discussion).

On both sides of the gap there is a substantial rise of T_b towards the center, but on the eastern side there is a conspicuous cut–off around 3 mas from the center (dashed line in Figure 4.13). This cut–off is present at all four frequencies although the inner components (only visible at 22 and 43 GHz) exhibit again a rise in T_b even above the cut–off value. The value of the innermost component A15 falls significantly below the extrapolation of the curve defined by A12, A13 and A14.

In the logarithmic plot of the brightness temperature distribution along the eastern jet (Figure 4.13) the data points above the cut–off can well be approximated with a straight line[7]. A linear regression of the form $\log(T_b/10^9\,\mathrm{K}) = A + B \cdot \log(r/1\,\mathrm{mas})$ (see Table 4.12 for the fitted parameters A and B, as well as the theoretical brightness temperatures T_b^{theo} from the fitted relation) was performed. The quantity B determines the slope of the regression line in Figure 4.13. A is a measure for the offset between the four lines at the four frequencies. Physically, A is the brightness temperature in units of 10^9 K of a component at a distance of 1 mas, assuming the validity of a linear extrapolation of $\log T_b$. The application of the linear regression gives at all four frequencies very similar dependences of T_b on approximately the -4th power of the radius, a result that constrains the turnover frequency distribution along the jet:

Table 4.8: Brightness temperatures and related parameters at 5 GHz

Component	$T_b[10^9\mathrm{K}]$	$T_b^{\mathrm{theo}}[10^9\mathrm{K}]^{\mathrm{a}}$	τ
D	0.96 ± 0.03	–	–
C1	0.50 ± 0.03	–	–
C2	6.17 ± 0.74	–	–
C3	9.30 ± 0.58	–	–
A10	$(47.64 \pm 13.61)^{\mathrm{b}}$	1192.73 ± 131.57	3.22 ± 0.29
A9	714.60 ± 255.87	388.91 ± 38.14	-0.61 ± 0.12
A7/8	66.54 ± 8.80	126.61 ± 10.73	0.64 ± 0.11
A6	46.72 ± 11.81	46.78 ± 3.34	0.0 ± 0.1
A5	28.14 ± 8.17	23.16 ± 1.41	-0.19 ± 0.13
A4	11.02 ± 0.56	9.64 ± 0.45	-0.13 ± 0.07
A3	1.63 ± 0.07	3.40 ± 0.09	0.74 ± 0.04
A2	1.11 ± 0.06	1.368 ± 0.01	0.21 ± 0.04
A1	1.26 ± 0.04	0.624 ± 0.007	-0.7 ± 0.03

[a] Theoretical brightness temperatures, calculated from a power–law fit of the measured values farther out than 3 mas along the eastern jet.
[b] Values in brackets are not used for the power–law fit.

Along a jet the flux density is proportional to $(\nu - \nu_t)^\alpha$ with ν fixed. If the turnover

[6] This corresponds to the FWHM of a circular Gaussian model component.

[7] No detailed examination of the brightness temperature distribution along the western jet is presented, since this suffers from the large gaps between the components and their small number.

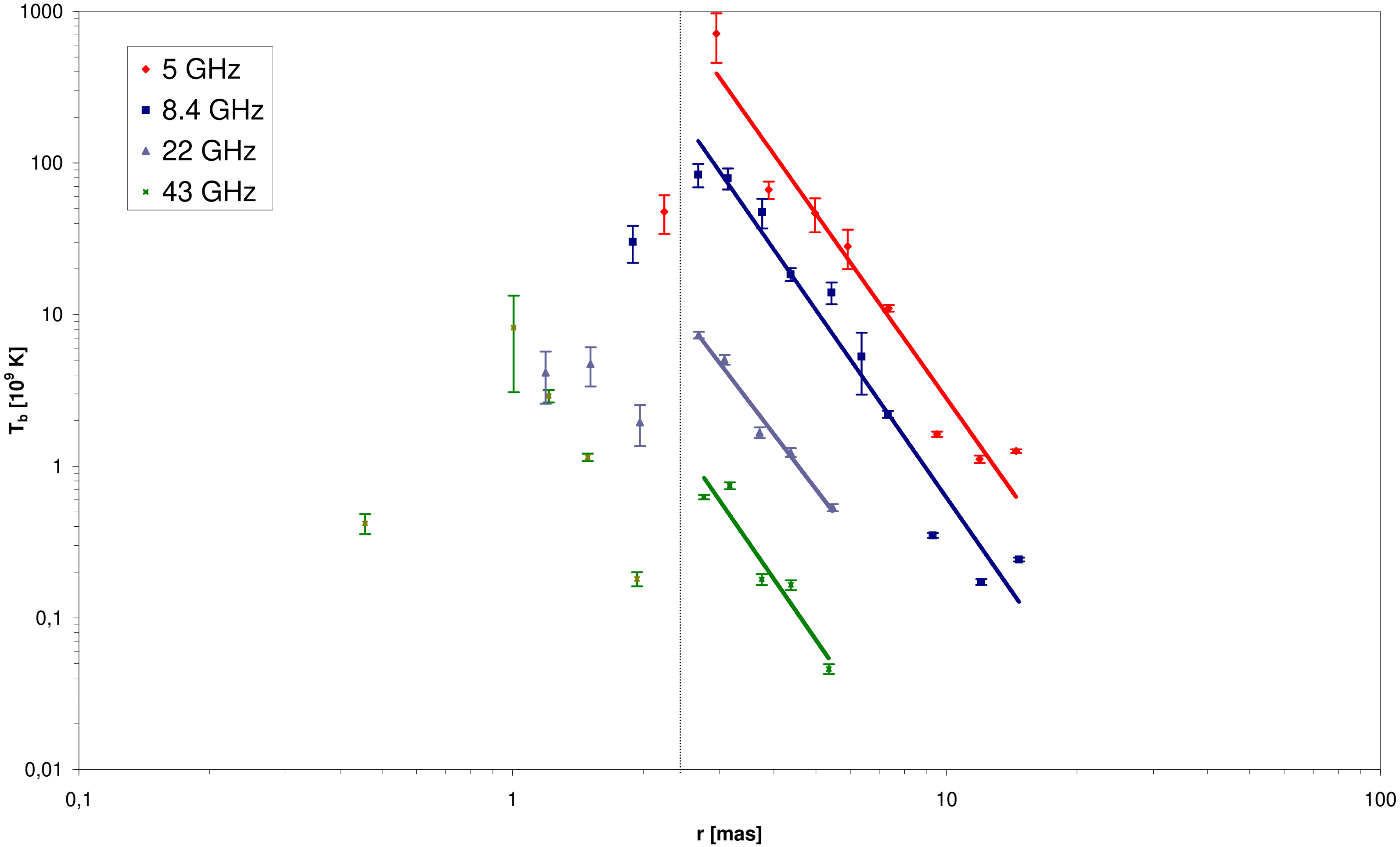

Figure 4.13: Logarithmic representation of the brightness temperature distribution along the eastern jet of NGC 1052. Above the cut–off distance the data can be fitted by a straight line (see Table 4.12 for the linear regression parameters) with a slope of ~ -4. The offset between the four data sets of brightness temperatures reflects the frequency dependence of T_b (see 4.1).

Table 4.9: Brightness temperatures and related parameters at 8.4 GHz

Component	$T_b [10^9 \mathrm{K}]$	$T_b^{\mathrm{theo}} [10^9 \mathrm{K}]^{\mathrm{a}}$	τ
D	0.251 ± 0.008	–	–
C1	0.19 ± 0.01	–	–
C2	2.43 ± 0.27	–	–
C3	4.63 ± 0.35	–	–
B1	7.70 ± 0.73	–	–
B2a/b	11.02 ± 1.00	–	–
A11	$(30.23 \pm 8.32)^{\mathrm{b}}$	590.18 ± 43.64	2.97 ± 0.2
A10	83.88 ± 14.88	141.47 ± 8.69	0.52 ± 0.16
A9	79.44 ± 12.57	74.30 ± 4.11	-0.07 ± 0.08
A8	47.51 ± 10.51	35.03 ± 1.68	-0.3 ± 0.07
A7	18.45 ± 1.81	18.82 ± 0.77	0.02 ± 0.07
A6	14.00 ± 2.31	7.72 ± 0.23	-0.6 ± 0.08
A5	5.28 ± 2.31	4.01 ± 0.09	-0.27 ± 0.11
A4	2.20 ± 0.12	2.26 ± 0.03	0.02 ± 0.05
A3	0.35 ± 0.01	0.849 ± 0.002	0.89 ± 0.03
A2	0.172 ± 0.008	0.294 ± 0.007	0.53 ± 0.04
A1	0.242 ± 0.007	0.129 ± 0.005	-0.63 ± 0.05

[a] Theoretical brightness temperatures, calculated from a power–law fit of the measured values farther out than 3 mas along the eastern jet.
[b] Values in brackets are not used for the power–law fit.

Table 4.10: Brightness temperatures and related parameters at 22 GHz

Component	$T_b [10^9 \mathrm{K}]$	$T_b^{\mathrm{theo}} [10^9 \mathrm{K}]^{\mathrm{a}}$	τ
C3b	0.08 ± 0.01	–	–
C3a	0.55 ± 0.05	–	–
B1	1.28 ± 7.26	–	–
B2a	6.68 ± 0.77	–	–
B2b	28.76 ± 1.81	–	–
A13	$(4.15 \pm 1.56)^{\mathrm{b}}$	153.54 ± 6.27	3.61 ± 0.26
A12	$(4.73 \pm 1.37)^{\mathrm{b}}$	62.80 ± 2.19	2.59 ± 0.18
A11	$(1.95 \pm 0.59)^{\mathrm{b}}$	23.46 ± 0.67	2.49 ± 0.18
A10	7.35 ± 0.37	7.31 ± 0.15	0.00 ± 0.04
A9	5.05 ± 0.38	4.38 ± 0.07	-0.14 ± 0.05
A8	1.67 ± 0.14	2.17 ± 0.02	0.27 ± 0.05
A7	1.23 ± 0.08	1.17 ± 0.002	-0.05 ± 0.05
A6	0.53 ± 0.03	0.508 ± 0.004	-0.05 ± 0.04

[a] Theoretical brightness temperatures, calculated from a power–law fit of the measured values farther out than 3 mas along the eastern jet.
[b] Values in brackets are not used for the power–law fit.

frequency ν_t varies as r^{-t}, with $t \geq 1$, a component further out is expected to have a lower flux density since the observing frequency is farther from the turnover frequency than for a component which is located at a smaller distance r. The flux density thus varies as $S_\nu \propto (r^{-t})^\alpha = r^{\alpha - t}$. If the jet has a constant opening angle, the diameters θ of the model components vary as $\theta \propto r$, leading to an overall dependence of $T_b \propto r^{\alpha - t - 2}$ of the brightness temperature on the distance from the center of jet activity. The spectral indices of the model components in the eastern jet scatter around -1 (see Figure 4.11). The measured dependence of T_b on the -4th power of r thus implies, that $t = 1$ (assuming, that the jet–axis lies in the plain of the sky, as suggested by the kinematical studies at 2 cm by Vermeulen et al. 2002), i.e. the turnover frequency varies as $\nu_t \propto r^{-1}$ along the eastern jet.

The linear regression fit parameters to the brightness temperatures as a function of

Table 4.11: Brightness temperatures and related parameters at 43 GHz

Component	$T_b[10^9\text{K}]$	$T_b^{\text{theo}}[10^9\text{K}]$[a]	τ
C3b	0.029 ± 0.003	–	–
B2a	0.62 ± 0.05	–	–
B2b	4.37 ± 0.05	–	–
A15	(0.42 ± 0.06)[b]	1446.63 ± 233.72	8.15 ± 0.17
A14	(8.21 ± 5.14)[b]	55.08 ± 4.24	1.90 ± 0.08
A13	(2.91 ± 0.28)[b]	25.55 ± 1.60	2.17 ± 0.08
A12	(1.15 ± 0.07)[b]	10.86 ± 0.52	2.25 ± 0.06
A11	(0.18 ± 0.02)[b]	3.65 ± 0.10	3.01 ± 0.06
A10	0.63 ± 0.02	0.839 ± 0.004	0.29 ± 0.01
A9	0.74 ± 0.04	0.476 ± 0.009	-0.45 ± 0.03
A8	0.18 ± 0.01	0.236 ± 0.009	0.28 ± 0.06
A7	0.16 ± 0.01	0.125 ± 0.007	-0.28 ± 0.07
A6	0.046 ± 0.003	0.054 ± 0.005	0.16 ± 0.10

[a] Theoretical brightness temperatures, calculated from a power–law fit of the measured values farther out than 3 mas along the eastern jet.
[b] Values in brackets are not used for the power–law fit.

Table 4.12: Linear regression parameters for the brightness temperature distribution along the eastern jet. The linear regression was applied to the values of $\log T_b$ as a function of $\log r$: $\log(T_b/10^9\,\text{K}) = A + B \cdot \log(r/1\,\text{mas})$.

Frequency	A	B
5 GHz	4.49 ± 0.33	-4.05 ± 0.39
8.4 GHz	3.91 ± 0.25	-4.11 ± 0.31
22 GHz	2.47 ± 0.19	-3.75 ± 0.32
43 GHz	1.75 ± 0.44	-4.14 ± 0.75

distance from the jet origin can be used to examine the frequency dependence of the determined T_b-data sets. From Equation (4.1) a dependence of $T_b \propto \nu^{-2+\overline{\alpha}}$ is expected, with an average spectral index $\overline{\alpha}$ along the jet. To analyze the dependence of A with frequency a linear regression of the form $A = A' + B' \cdot \log(\nu/1\,\text{Hz})$ was performed. This gave $B' = -3.02 \pm 0.14$ implying a dependence of $T_b \propto \nu^{-3.02\pm0.14}$. The best value for the average spectral index is thus $\alpha_{mean} = -1.02 \pm 0.14$. The plot of the linear regression in Figure 4.14 demonstrates the quality of the fit and shows that -1 is a reasonable estimate of the intrinsic spectral index along the eastern jet of NGC 1052. Therefore, the energy distribution of the electrons follows a power-law with an index of $s_{mean} = 1 - 2\alpha_{mean} = 3.04 \pm 0.28$.

If the maximal brightness temperature of the jet were constant along the jet, a set of measurements of T_b and the spectral indices α of the model components could be used to derive the precise turnover frequency distribution in the jet. As a natural choice for the maximal T_b, the cut–off brightness temperature measured at 5 GHz can be used. For each component a factor can be calculated, by which the measured value of T_b has to be multiplied to reach the maximal value. The small value measured for T_b can be attributed to the shape of the corresponding model component spectrum. Assuming an optically thin spectrum with a spectral index α measured at the corresponding frequency, the turnover frequency (at which the maximal value should be reached) can be calculated from the correction factor. The application of this idea leads to a turnover frequency distribution along the jet for each frequency data set. However, offsets between the four curves reflect the fact that the maximal brightness temperature along the eastern jet of NGC 1052 is

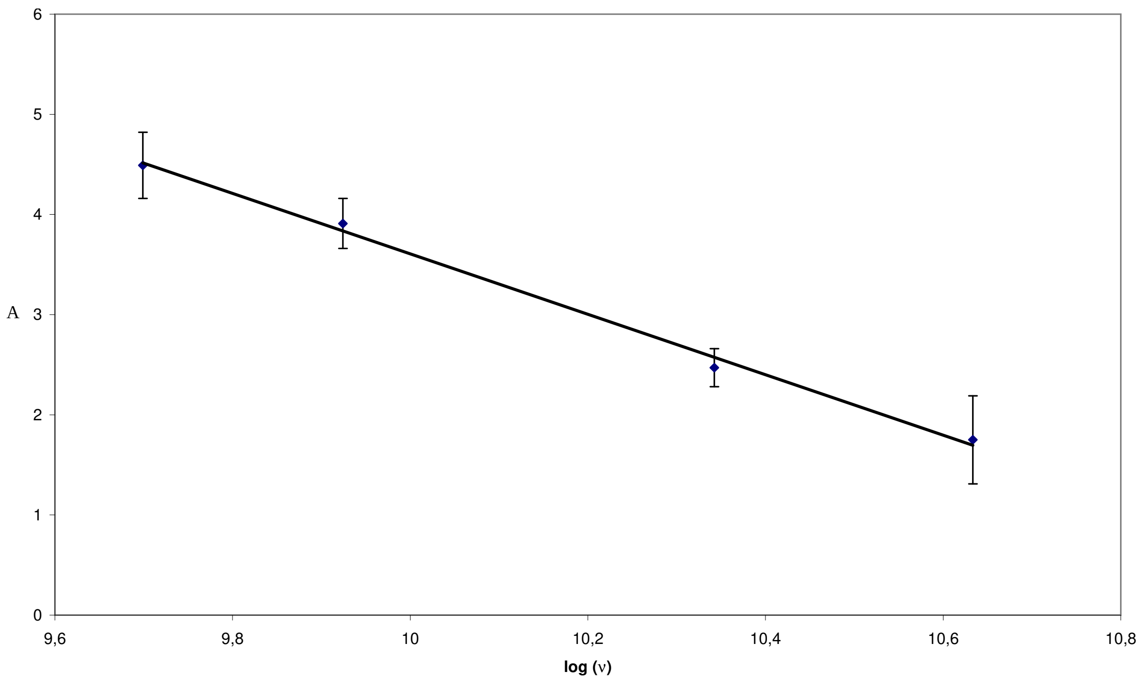

Figure 4.14: Frequency dependence of the brightness temperatures in the eastern jet of NGC 1052. The value of A ($\hat{=} \log T_b(r = 1\,\mathrm{mas})$ assuming a linear extrapolation of the linear regression line) is plotted as a measure for the relative offset between the four T_b-data sets as a function of frequency. The fitted dependence of $r^{-3.02\pm0.14}$ indicates an average spectral index of ~ -1 along the eastern jet (see text).

not constant. It is not possible to find a consistent model with just one maximal value of T_b, i.e., there is an evolution of the maximal brightness temperature with distance. A more detailed model of this evolution should in principle be able to reproduce consistent values of ν_t, from all four data sets, but this will be kept for later efforts.

The frequency–independence of the cut–off distance of 3 mas implies an external effect suggesting that at this position the influence of the nuclear absorber starts to affect substantially the jet and the brightness temperature of its components. This suggests the presence of an obscuring torus around the central engine of NGC 1052 with a sharp edge, rather than a circumnuclear cloud system. To check this hypothesis it was tested if the free-free absorber model can cause the observed cut–off in the brightness temperature distribution. In the case of free-free absorption, the observed flux density $S_{\nu,\mathrm{abs}}$ should depend on the intrinsic flux density S_ν, the optical depth of the absorber τ_f and the observing frequency ν as

$$S_{\nu,\mathrm{abs}} = S_\nu \cdot e^{-\tau_f} \tag{4.2}$$

From this equation, the optically depth of the absorber, needed to change the theoretical value (extrapolation of the linear regression line) to the measured one, can be calculated. This calculation can be done for A10 at 5 GHz, for A11 at 8.4 GHz, for A11, A12 and A13 at 22 GHz, and finally for A11, A12, A13, A14 and A15 at 43 GHz. The calculated values are given in Table 4.13. At each of the three highest frequencies it turns out that the resulting values for τ_f are very similar within one dataset except the one for the innermost component which has a significantly higher optically depth. This larger value can be explained in terms of additional synchrotron self absorption, so that the measured optically depth is a superposition of two distinct contributions $\tau = \tau_f + \tau_s$, expected at the most compact component in a jet.

Assuming an absorbing pathlength of 0.3 pc (comparable to the extent of the absorbing region in the plane of the sky), the obtained opacities constrain the physical properties in the torus. Equation (2.28) can be simplified to

$$\begin{aligned} \tau_f &= 30 \cdot 10^{16}\, L\, T^{-1.35}\, \nu^{-2.1}\, \overline{n}^2 \\ \Rightarrow \quad T^{-1.35}\, \overline{n}^2 &= 3.33 \cdot 10^{-18}\, L^{-1} \tau_f\, \nu^{2.1} \end{aligned}$$

with a length $L = \int dl$ and an average density $\overline{n}$. For $\tau_f \sim 2.5$ at $\nu = 22\,\mathrm{GHz}$ at a temperature of $T = 10^4\,\mathrm{K}$, this results to a density of $\overline{n} = 6 \cdot 10^5\,\mathrm{cm}^{-3}$ and an absorbing column density of $5.6 \cdot 10^{22}\,\mathrm{cm}^{-2}$. This value is consistent with the implications of the X-ray observations of NGC 1052, which find a (model-dependent) column density of 10^{22}-$10^{23}\,\mathrm{cm}^{-2}$ towards the unresolved nuclear X-ray core (Appendix D; compare also Weaver et al. 1999, Guainazzi & Antonelli 1999).

Table 4.13: Calculated values of τ. Note that the given error is a formal uncertainty. A more realistic value can be estimated from the scatter in Figure 4.15 to ~0.5.

ν	A10	A11	A12	A13	A14	A15
5 GHz	3.22 ± 0.29[a]	-	-	-	-	-
8.4 GHz	0.52 ± 0.16	2.97 ± 0.20[a]	-	-	-	-
22 GHz	0.00 ± 0.04	2.49 ± 0.18	2.59 ± 0.18	3.61 ± 0.26[a]	-	-
43 GHz	0.29 ± 0.02	3.00 ± 0.06	2.25 ± 0.06	2.17 ± 0.08	1.90 ± 0.08	8.15 ± 0.17[a]

[a] The jet core is likely to show a combination of self- and free-free absorption.

The results from the analysis of the brightness temperature distribution along the eastern jet draw a consistent picture of the situation at the center of NGC 1052. At the inner 3 mas of the eastern jet a free-free absorbing medium dominates the flux density properties. This absorber has a nearly sharp edge since its influence rises rapidly within one milliarcsecond, corresponding to less than 0.1 pc. The components which are visible nearer than 3 mas to the center are observed through this absorber and thus are substantially dimmed relative to their initial brightness. With the information of the absolute contribution of the obscuring torus and the knowledge of its spatial extent it will be possible to derive additional information about its density gradients in the analysis of the core–shift in Section 4.6 .

4.5 Polarimetry

The polarimetric information contained in the measurement of all four Stokes parameters can be used to image the polarized emission of the observed sources. The calibration method described in Section 3.3 makes it necessary to compare the derived electric vector position angles (EVPA) to other measurements in order to make sure that the polarization calibration worked properly. 3C 345, included as a calibrator source in the VLBA observations of NGC 1052, is very well suited for this purpose since a big 'database' exists in the literature from which the EVPA of the core and jet regions in this source can be obtained. Once the EVPA of 3C 345 at a special frequency and epoch is calibrated the corresponding rotation can be applied. The same rotation of the EVPA then has to be applied to the corresponding dataset of NGC 1052 at the same epoch and frequency.

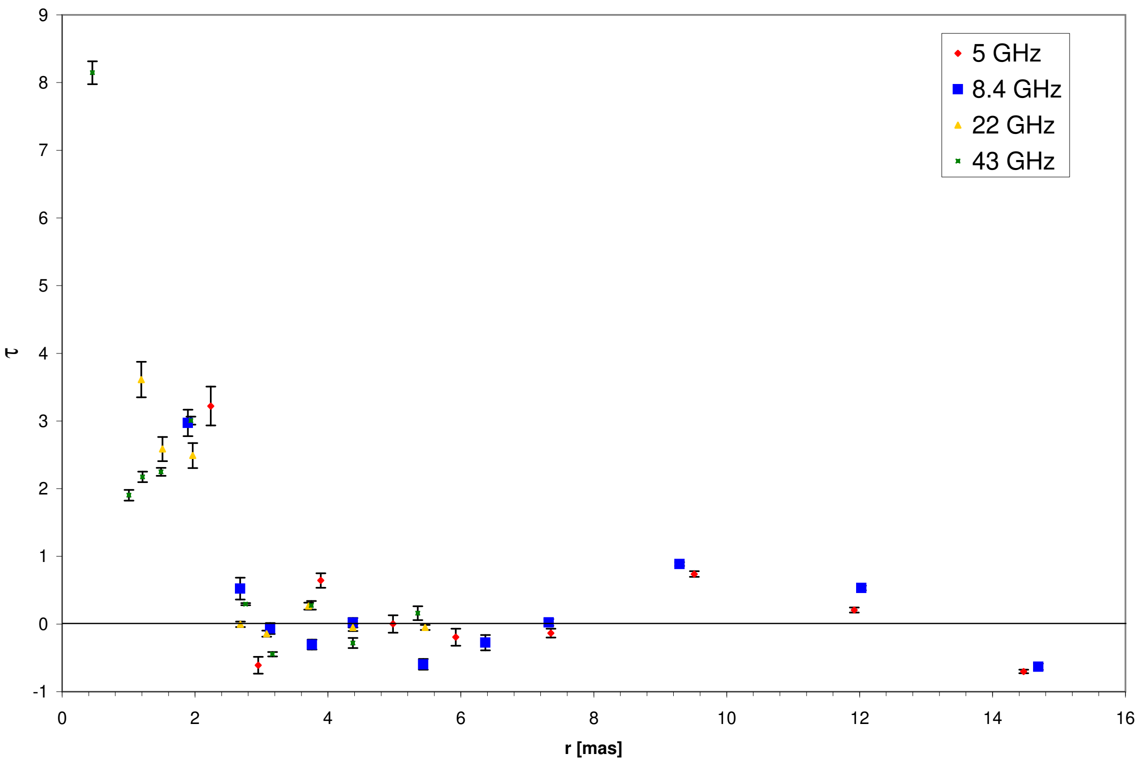

Figure 4.15: Calculated opacities along the eastern jet of NGC 1052.

3C 345 was mapped in DIFMAP using the automatic mapping scripts MUPPET and AUTOMAP developed by Shepherd and Taylor (for the CJ-survey). Special care was taken at 43 GHz where the same 'manual' mapping technique was used as for the target source NGC 1052 (see Section 3.3). The FITS-files were then read into $\mathcal{AIPS}$ and the mapping of the Q, U and V Stokes parameters was done. In this mapping procedure an antenna table was applied which contained the D-terms of the VLBA at the corresponding frequency, determined from NGC 1052 (Section 3.3). The maps of Q and U were combined using the task COMB. The linearly polarized intensity and the EVPA are presented in Figure 4.16. It should be mentioned that these maps are only a by-product of the target observation of NGC 1052 and are based only on two scans of 5 minutes each at all frequencies. 3C 345 shows a core-jet structure with 3 main components at 43 GHz.

It is known that the EVPA in 3C 345 is highly variable at 5 GHz in the core region but stable at the two extended jet regions starting at ∼3 mas from the core, where the EVPA is roughly parallel to the jet. This is in good agreement with the EVPA in these regions in Figure 4.16. Therefore, no EVPA rotation was necessary from the polarization calibration at this frequency.

At 8.4 GHz the situation is more difficult since no stable region of EVPA is known at this frequency in 3C 345. For the calibration of the EVPA the single dish results from the Michigan database (accessible via the Internet at the URL: `http://www.astro.lsa.umich.edu-/obs/radiotel/umrao.html`) were used. A rotation of the electric vector of -73° was needed. At 22 and 43 GHz the D-term results from the 3C 120 monitoring from Gómez et al. (2000) were used. No correction of the EVPA at 43 GHz had to be applied. At 22 GHz a rotation about -75° was necessary.

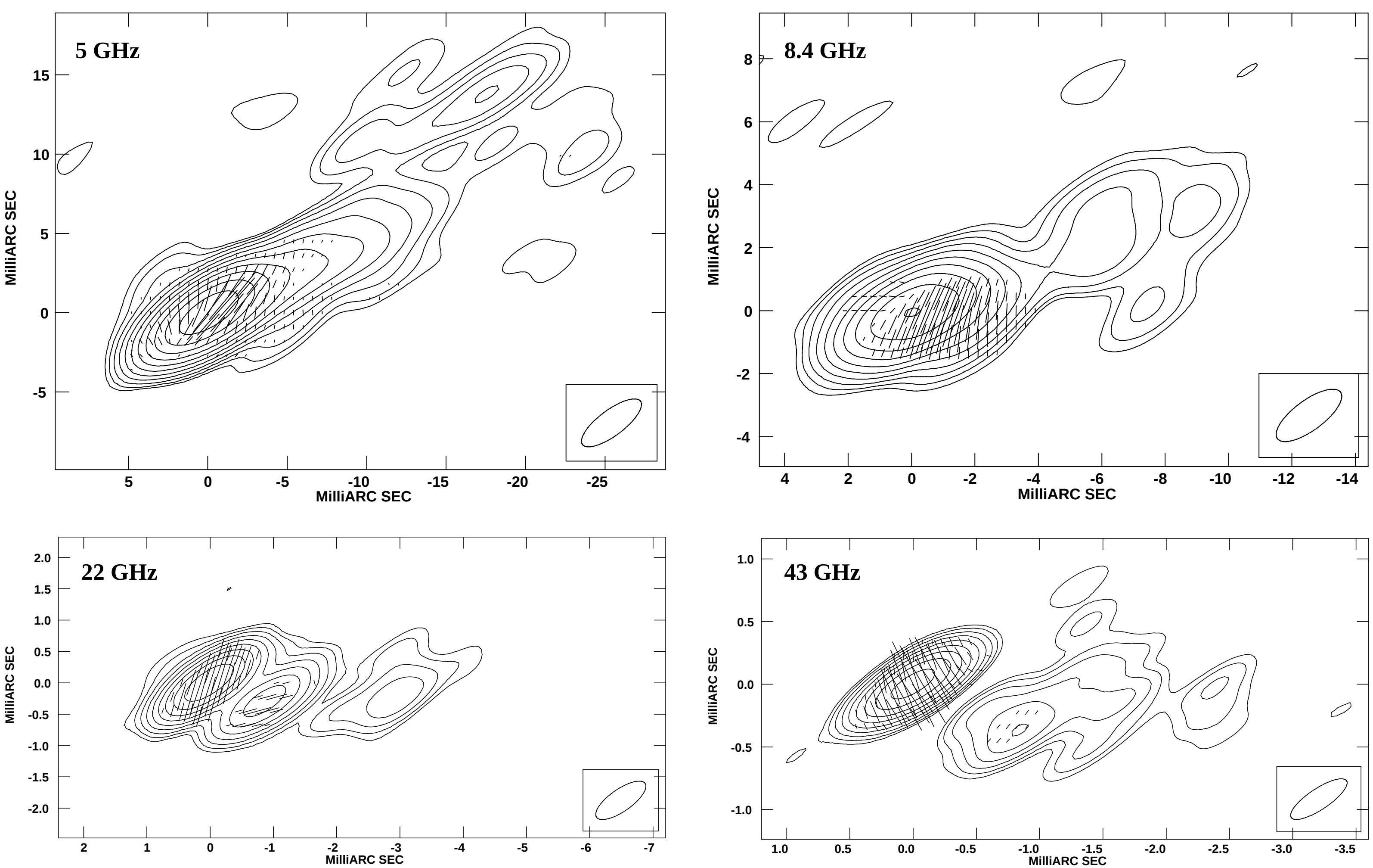

Figure 4.16: Polarized emission images of 3C 345 at 5, 8.4, 22 and 43 GHz. The total intensity is shown in contours. Superimposed, the EVPAs are shown, with a length proportional to the linearly polarized intensity. The contour level intervals are 3, 8, 10 and 8 mJy at 5, 8.4, 22 and 43 GHz, and a length of 1 mas of the EVPA corresponds to 33, 67, 133 and 267 mJy, respectively.

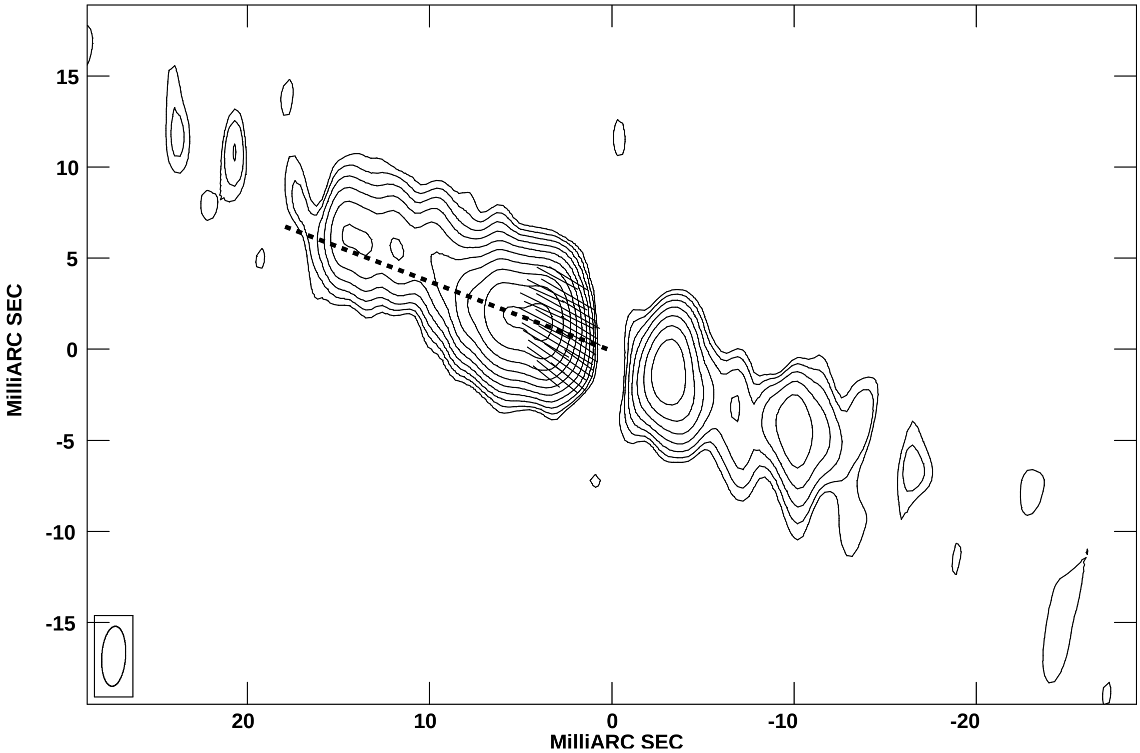

Figure 4.17: The C–band map of the polarized emission in NGC 1052.

The maps in Figure 4.16 are χ-corrected and thus show the true polarimetric structure of 3C 345 at epoch 1998.99.

NGC 1052 was mapped in all four Stokes parameters according to the procedure described in Section 3.3 . Figure 4.17 shows the linearly polarized intensity and its EVPA overlaid on the total intensity at 5 GHz. A region of linearly polarized emission is visible at the base of the eastern jet. The peak is about 3 mJy per beam and the EVPA is about 70°, roughly parallel to the jet. This indicates an ordered magnetic field perpendicular to the jet axis, if no Faraday rotation is assumed. To decide whether the region of linearly polarized emission is resolved or unresolved, a slice through jet axis of both the total intensity map and the polarization map was produced, using the task SLICE in $\mathcal{AIPS}$ (Figure 4.18). In this plot the polarized emission peaks about 1 mas offset from the total intensity maximum. A comparison to Figure 4.3 ascribes this part of the jet to component A10, which is optically thick at 5 GHz. A weak asymmetry of the polarized emission slice suggests a contribution of at least two components. The polarized emission is thus slightly resolved and originates in the optically thick part of the eastern jet at 5 GHz.

No linearly polarized emission from NGC 1052 could be detected at the other three frequencies. Usually the degree of polarization rises with frequency[8] and thus it would be expected that the eastern jet should exhibit polarized emission from the region around component A10 and A11 also at 8.4 GHz. Having the polarization the same (flat) spectrum

[8] Beam depolarization should lower the degree of polarization at the lower frequency much stronger than at the higher frequency, due to the different beam sizes.

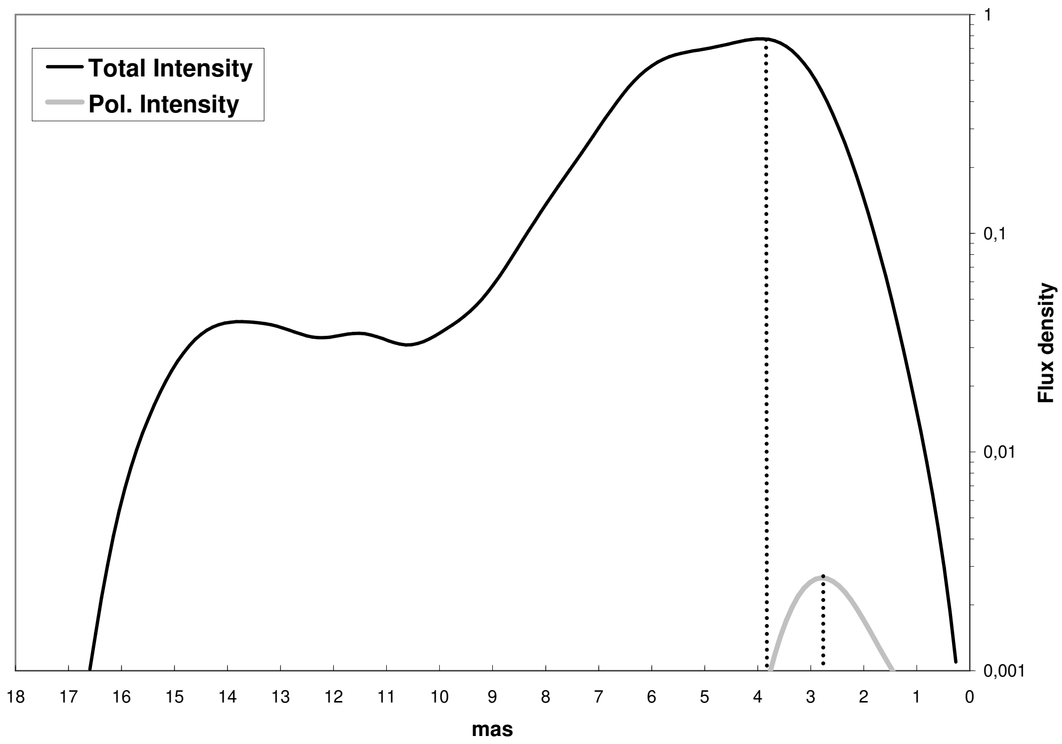

Figure 4.18: Slice through the total intensity and polarized emission along the eastern jet of NGC 1052 at 5 GHz.

as the total intensity in this regime, it should reach a value of about 3 mJy per beam at 8.4 GHz (comparable to the polarized flux at 5 GHz). At higher frequencies these components become optically thin and thus fall in total intensity. If their emission is polarized to the same degree than at 5 GHz this would correspond to less than 1 mJy and thus below the detection threshold.

The simplest explanation for this behavior of the linearly polarized emission from this jet-region is, that the different layers of the jet have a different degree of polarization. Since the region around component A10 is optically thick at 5 GHz, the detected emission originates in an outer layer of the jet. If this outer layer is polarized to a higher degree than the inner layers of the jet, one indeed expects no polarized emission at 8.4 GHz, where the region around A10 is optically thin and we are observing a much deeper region of the jet. However, this raises the question, why the region around A11 appears to be unpolarized, which is still optically thick at 8.4 GHz. In principle the higher column density at this more central region could cause higher Faraday depolarization than it does at the region around A10. This idea is supported by the fact that A10 is the first component which seems to be affected by strong free-free absorption (see Section 4.4). In this scenario the radiation from the outer jet layers is intrinsically linearly polarized. Inside a radius of 3 mas however, Faraday depolarization inside a central torus makes the radiation appear unpolarized. This scenario needs to be tested with observations at longer wavelengths and especially around 5 GHz, where the depolarization is expected to start dominating.

4.6 Core shift analysis

The symmetry between the jet and the counterjet constrains the position of the central engine in NGC 1052. The core of both jets (compare Section 2.2.3 for a definition of the term "core") are located at the distances to the central engine r_c, where the optical depth τ has fallen to be ~ 1. This distance is given by: $r_c \sim \nu^{-\frac{1}{k_r}}$, where $k_r = ((3-2\alpha)m + 2n - 2)/(5-2\alpha)$, with m and n the power indices of the magnetic field and the particle density: $B \sim r^{-m}$, $N \sim r^{-n}$ (Lobanov 1998). Taking logarithms leads to:

$$\log(r_c) = \text{const.} - \frac{1}{k_r} \cdot \log(\nu).$$

Measuring r_c at two frequencies allows one to determine k_r in the corresponding region of the jet. For a freely expanding jet in equipartition Blandford & Königl (1979), k_r=1. The value of k_r is larger in regions with steep pressure gradients and may reach 2.5, for reasonable values of m, n ($\leq$4, see Lobanov 1998). If external absorption determines the apparent core position, comparable density gradients of the external medium can alter k_r to values above 2.5 (see Section 2.2.3 for details).

The values of k_r deduced depend crucially on the absolute values of r_c on the two sides and therefore on the assumed position of the central engine. Four scenarios have been tested with different reference points (see Figure 4.19). Table 4.14 gives the derived values of k_r for each scenario.

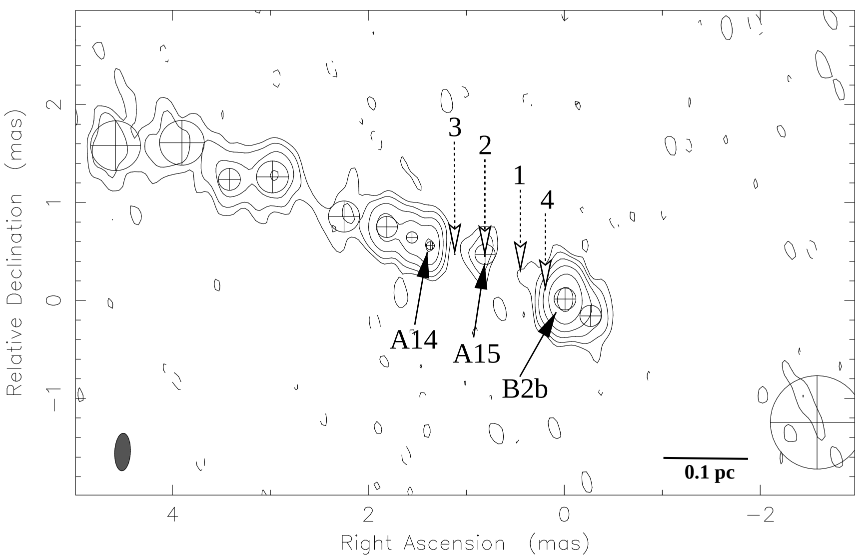

Figure 4.19: Image with the model fitting results of the 43 GHz data. The circles represent the Gaussian components. The innermost jet components are labeled as A14, A15 and B2b. The putative locations of the central engine are indicated (dashed arrows) for 4 different scenarios (see discussion in the text).

The area between the model components A15 and B2b is the most likely location of the central engine and the center between both components is a natural choice for its exact position (scenario 1). Shifting the reference point eastwards (scenarios 2 and 3) alters the values of k_r into unphysically large regimes (requiring density gradients $\propto r^{-10}$ and higher). Assuming the true center of activity to be located more westwards (closer to B 2b, scenario 4), the values of k_r derived are still acceptable.

Table 4.14: k_r values for the four different putative centers of activity.

ν [GHz]	—Scenario 1— $k_{r,\text{east}}$	$k_{r,\text{west}}$	—Scenario 2— $k_{r,\text{east}}$	$k_{r,\text{west}}$	—Scenario 3— $k_{r,\text{east}}$	$k_{r,\text{west}}$	—Scenario 4— $k_{r,\text{east}}$	$k_{r,\text{west}}$
5–8.4	3.1±2.6	–	2.5±2.2	–	3.0±3.6	–	3.4±2.8	–
8.4–22	2.1±0.5	6.6±2.8	1.5±0.3	11.9±5.1	1.0±0.2	14.8±6.2	2.4±0.6	3.8±1.6
22–43	3.9±0.8	6.8±2.7	2.4±0.5	13.0±5.2	1.3±0.2	17.1±7.1	4.8±1.0	3.6±1.3

The core positions of both jets at the different frequencies for the first case (scenario 1) are shown in Figure 4.20. The eastern jet has rather high values of k_r below 22 GHz, although still in agreement with steep pressure gradients in the jet environment. Above 22 GHz k_r is 3.9±0.8, which is a good indicator for free-free absorption affecting the jet opacity. The western jet has values of k_r as high as 6.8±2.7 between 22 and 43 GHz, suggesting a large contribution from free–free absorption.

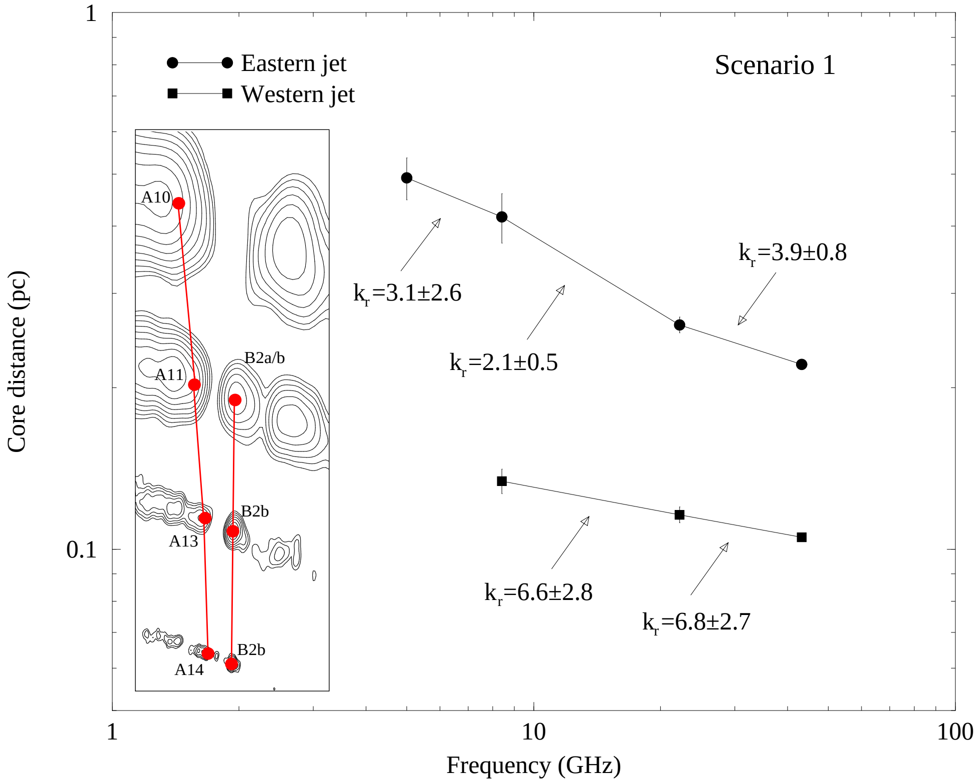

Figure 4.20: Core positions in the two jets at the different frequencies for scenario 1 (see Figure 4.19). The corresponding values of k_r for the core–shift between adjacent frequencies are labeled. Smaller core–shifts correspond to higher values of k_r. Table 4.14 provides the values of k_r for the other three scenarios. The inlaid panel shows the core-locations in the source at the four frequencies (from top to bottom at 5, 8.4, 22 and 43 GHz).

The results from the core–shift analysis support the picture of a free–free absorbing torus covering mainly the inner part of the western jet and also a smaller fraction of the eastern jet. The extend of this torus along the eastern jet is consistent with the results derived from the analysis of brightness temperature distribution (Section 4.4). The true center of activity in NGC 1052 can be determined to lie between the model components A 15 and B 2b, with an uncertainty of only ~ 0.03 pc.

Bibliography

Barth, A. J., Filippenko, A. V., & Moran, E. C. 1999, Astrophys. J., 515, L61

Becklin, E. E., Tokunaga, A. T., & Wynn-Williams, C. G. 1982, Astrophys. J., 263, 624

Blandford, R. D. & Königl, A. 1979, Astrophys. J., 232, 34

Blumenthal, G. R. & Gould, R. J. 1970, Reviews of Modern Physics, 42, 237

Braatz, J. A., Wilson, A. S., & Henkel, C. 1996, Astrophys. J. Suppl., 106, 51

Brown, R. L. 1987, in Spectroscopy of Astrophysical Plasmas, 35–58

California Institute of Technology. 1991, BAAS, 23, 991

Claussen, M. J., Diamond, P. J., Braatz, J. A., Wilson, A. S., & Henkel, C. 1998, Astrophys. J., 500, L129

Condon, J. J., Condon, M. A., Gisler, G., & Puschell, J. J. 1982, Astrophys. J., 252, 102

Daly, R. A. & Marscher, A. P. 1988, Astrophys. J., 334, 539

de Vries, W. H., Barthel, P. D., & O'Dea, C. P. 1997, Astron. & Astrophys., 321, 105

Eckart, A. & Genzel, R. 1996, Nature, 383, 415

Falcke, H. & Biermann, P. L. 1995, Astron. & Astrophys., 293, 665

Falcke, H., Wilson, A. S., & Simpson, C. 1998, Astrophys. J., 502, 199

Fomalont, E. 1981, Newsletter. NRAO No. 3, p. 3, 1981, 3, 3

Forbes, D. A., Georgakakis, A. E., & Brodie, J. P. 2001, Monthly Not. Roy. Astron. Soc., 325, 1431

Fosbury, R. A. E., Mebold, U., Goss, W. M., & Dopita, M. A. 1978, Monthly Not. Roy. Astron. Soc., 183, 549

Gómez, J. L., Marscher, A. P., Alberdi, A., Jorstad, S. G., & García-Miró, C. 2000, Science, 289, 2317

Gabel, J. R., Bruhweiler, F. C., Crenshaw, D. M., Kraemer, S. B., & Miskey, C. L. 2000, Astrophys. J., 532, 883

Gallagher, J. S. 1986, Publ. Astron. Soc. Pacific, 98, 81

Georganopoulos, M. & Marscher, A. P. 1996, in ASP Conf. Ser. 100: Energy Transport in Radio Galaxies and Quasars, 67

Guainazzi, M. & Antonelli, L. A. 1999, Monthly Not. Roy. Astron. Soc., 304, L15

Guainazzi, M., Oosterbroek, T., Antonelli, L. A., & Matt, G. 2000, Astron. & Astrophys., 364, L80

Harris, D. E., Carilli, C. L., & Perley, R. A. 1994, Nature, 367, 713

Harris, D. E. & Krawczynski, H. 2002, Astrophys. J., 565, 244

Heeschen, D. S. 1970, Astron. J., 75, 523

Heeschen, D. S. & Puschell, J. J. 1983, Astrophys. J., 267, L11

Ho, L. C., Filippenko, A. V., & Sargent, W. L. 1995, Astrophys. J. Suppl., 98, 477

Ho, L. C., Filippenko, A. V., & Sargent, W. L. W. 1997, Astrophys. J. Suppl., 112, 315

Högbom, J. A. 1983, in Indirect Imaging. Measurement and Processing for Indirect Imaging. Proceedings of an International Symposium held in Sydney, Australia, August 30-September 2, 1983. Editor, J.A. Roberts; Publisher, Cambridge, England, New York, USA, Cambridge University Press, 1984, 247

Johnston, K. J., Fey, A. L., Zacharias, N., Russell, J. L., Ma, C., de Vegt, C., Reynolds, J. E., Jauncey, D. L., Archinal, B. A., Carter, M. S., Corbin, T. E., Eubanks, T. M., Florkowski, D. R., Hall, D. M., McCarthy, D. D., McCulloch, P. M., King, E. A., Nicolson, G., & Shaffer, D. B. 1995, Astron. J., 110, 880

Jones, D. L., Tingay, S. J., Murphy, D. W., Meier, D. L., Jauncey, D. L., Reynolds, J. E., Tzioumis, A. K., Preston, R. A., McCulloch, P. M., Costa, M. E., Kemball, A. J., Nicolson, G. D., Quick, J. F. H., King, E. A., Lovell, J. E. J., Clay, R. W., Ferris, R. H., Gough, R. G., Sinclair, M. W., Ellingsen, S. P., Edwards, P. G., Jones, P. A., van Ommen, T. D., Harbison, P., & Migenes, V. 1996, Astrophys. J., 466, L63

Jones, D. L., Wehrle, A. E., Meier, D. L., & Piner, B. G. 2000, Astrophys. J., 534, 165

Jones, D. L., Wrobel, J. M., & Shaffer, D. B. 1984, Astrophys. J., 276, 480

Kameno, S., Sawada-Satoh, S., Inoue, M., Shen, Z., & Wajima, K. 2001, Publ. Astron. Soc. Japan, 53, 169

Kellermann, K. I., Vermeulen, R. C., Cohen, M. H., & Zensus, J. A. 1999, in American Astronomical Society Meeting, Vol. 194, #20.02

Kellermann, K. I., Vermeulen, R. C., Zensus, J. A., & Cohen, M. H. 1998, Astron. J., 115, 1295

Kemball, A. J., Diamond, P. J., & Cotton, W. D. 1995, Astron. &. Astrophys. Suppl., 110, 383

Knapp, G. R., Faber, S. M., & Gallagher, J. S. 1978, Astron. J., 83, 139

Krichbaum, T. P., Alef, W., Witzel, A., Zensus, J. A., Booth, R. S., Greve, A., & Rogers, A. E. E. 1998, Astron. & Astrophys., 329, 873

Krolik, J. H. 1999, Active galactic nuclei : from the central black hole to the galactic environment (Princeton, NJ, USA : Princeton University Press, 1999.)

Leppänen, K. J., Zensus, J. A., & Diamond, P. J. 1995, Astron. J., 110, 2479

Levinson, A., Laor, A., & Vermeulen, R. C. 1995, Astrophys. J., 448, 589+

Lobanov, A. P. 1998, Astron. & Astrophys., 330, 79

Marr, J. M., Taylor, G. B., & Crawford, F. 2000, in Astrophysical Phenomena Revealed by Space VLBI, Proceedings of the VSOP Symposium, held at the Institute of Space and astronautical Science, Sagamihara, Kanagawa, Japan, January 19 - 21, 2000, Eds.: H. Hirabayashi, P.G. Edwards, and D.W. Murphy, Sagamihara, Kanagawa, Japan: Institute of Space and astronautical Science, 2000, 91

Mayall, N. U. 1939, Lick Observatory Bulletin, 497, 33

McDowell, J. C. 1994, in Einstein Obs. Unscreened IPC Data Archive

Mirabel, I. F. & Rodríguez, L. F. 1999, Annu. Rev. Astron. Astrophys., 37, 409

Miyoshi, M., Moran, J., Herrnstein, J., Greenhill, L., Nakai, N., Diamond, P., & Inoue, M. 1995, Nature, 373, 127

Napier, P. J. 1994, in IAU Symp. 158: Very High Angular Resolution Imaging, Vol. 158, 117

Omar, A., Anantharamaiah, K. R., Rupen, M., & Rigby, J. 2002, Astron. & Astrophys., 381, L29

Pearson, T. J., Shepherd, M. C., Taylor, G. B., & Myers, S. T. 1994, in American Astronomical Society Meeting, Vol. 185, #08.08

Peterson, B. M. 1997, An introduction to active galactic nuclei (Cambridge, UK, New York, USA: Cambridge University Press)

Pogge, R. W., Maoz, D., Ho, L. C., & Eracleous, M. 2000, Astrophys. J., 532, 323

Ros, E. 1997, Astrometría diferencial de precisión con VLBI en el triángulo de Draco (y estudios de SN 1993J) (València, Spain: Servicio de Publicaciones, Universitat de València), 35

Rybicki, G. B. & Lightman, A. P. 1979, Radiative Processes in Astrophysics (New York, USA: Wiley-Interscience)

Schwartz, D. A., Marshall, H. L., Lovell, J. E. J., Piner, B. G., Tingay, S. J., Birkinshaw, M., Chartas, G., Elvis, M., Feigelson, E. D., Ghosh, K. K., Harris, D. E., Hirabayashi, H., Hooper, E. J., Jauncey, D. L., Lanzetta, K. M., Mathur, S., Preston, R. A., Tucker, W. H., Virani, S., Wilkes, B., & Worrall, D. M. 2000, Astrophys. J., 540, L69

Smith, D. A., Wilson, A. S., Arnaud, K. A., Terashima, Y., & Young, A. J. 2002, Astrophys. J., 565, 195

Thompson, A. R., Moran, J. M., & Swenson, G. W. 1986, Interferometry and synthesis in radio astronomy (New York, Wiley-Interscience)

Tingay, S. J. & Murphy, D. W. 2001, Astrophys. J., 546, 210

Van Gorkom, J. H., Knapp, G. R., Raimond, E., Faber, S. M., & Gallagher, J. S. 1986, Astron. J., 91, 791

Vermeulen, R. C., Readhead, A. C. S., & Backer, D. C. 1994, Astrophys. J., 430, L41

Vermeulen, R. C., Ros, E., Kellermann, K. I., Cohen, M. H., & Zensus, J. A. 2002, in prep.

Wagner, S. J. & Witzel, A. 1995, Annu. Rev. Astron. Astrophys., 33, 163

Weaver, K. A., Wilson, A. S., Henkel, C., & Braatz, J. A. 1999, Astrophys. J., 520, 130

Wells, D. C., Greisen, E. W., & Harten, R. H. 1981, Astron. &. Astrophys. Suppl., 44, 363

Wilson, A. S. & Yang, Y. 2002, Astrophys. J., 568, 133

Wilson, A. S., Young, A. J., & Shopbell, P. L. 2000, Astrophys. J., 544, L27

Wrobel, J. M. 1984, Astrophys. J., 284, 531

Young, A. J., Wilson, A. S., Terashima, Y., Arnaud, K. A., & Smith, D. A. 2002, Astrophys. J., 564, 176

Yusef-Zadeh, F., Melia, F., & Wardle, M. 2000, Science, 287, 85

Zensus, J. A. 1997, Annu. Rev. Astron. Astrophys., 35, 607

Zensus, J. A., Ros, E., Kellermann, K. I., Cohen, M. H., Vermeulen, R. C., & Kadler, M. 2002, in press (Astron. J., issue August 2002)